Ocean Engineering 288 (2023) 116144

Contents lists available at ScienceDirect

Ocean Engineering

journal homepage: www.elsevier.com/locate/oceaneng

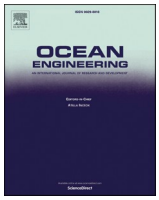

Wave overtopping of a vertical seawall in a surf zone: A joint analysis of numerical and laboratory data

Mariano Buccino [a,*], Angela Di Leo [b], Sara Tuozzo [a], Luìs F. Còrdova Lopez [c], Mario Calabrese [a], Fabio Dentale [b]

[a] Department of Civil, Architectural and Environmental Engineering, University of Napoli "Federico II", Via Claudio 21, 80125, Napoli, Italy
[b] Department of Civil Engineering, University of Salerno, Via Giovanni Paolo II, 132, 84084, Fisciano, Italy
[c] Centro de Investigaciones Hidráulicas, Universidad Tecnológica de La Habana "José Antonio Echeverría", Calle 114 entre Ciclovía y Rotonda, Marianao, La Habana, Cuba

ARTICLE INFO

Handling Editor: Prof. A.I. Incecik

Keywords:
Wave overtopping
RANS
SWASH
Physical modelling
Surf-zone wave spectra

ABSTRACT

This research uses physical and numerical experiments to investigate the wave overtopping of a vertical seawall in an uneven surf zone. The numerical experiments exploit two approaches, which differ in vertical resolution and computational time: CFD-RANS and SWASH. The tests were conducted with and without the wall, allowing the analysis of the spectral evolution in shallow water and its relationships with wave overtopping. The study assesses the performance of numerical models with different levels of complexity and uses laboratory and numerical data to understand the key variables that control the phenomena under study. The results indicate that while CFD-RANS is quantitatively in line with the laboratory measurements, SWASH overestimates the spectral moments and underpredicts the overtopping rate by a factor of 2. However, the numerical tools satisfactorily reproduce the physics of the processes, allowing us to focus on some aspects of engineering relevance. Laboratory and numerical data indicate that the overtopping rate depends not on the wave spectrum shape but on the high percentiles of the wave elevation distribution. This outcome clarifies that wave setup is a critical variable for prediction purposes.

Finally, the article highlights that the surf zone's spectral moments are correlated. The correlation structure is such that the mean spectral periods became proportional to the local wave energy despite these quantities being independent in deeper water. We warn that this phenomenon could result in spurious, unphysical relationships between mean spectral periods and overtopping rates. The analysis of further literature data corroborates this conclusion.

List of symbols

The following symbols are used in this paper (Fig. 1):

1. Introduction

Wave overtopping is a leading process in designing coastal structures to protect land from flooding and secure ships, people, and cargo in port areas. It is also one of the fundamental mechanisms for converting wave energy into electrical power. As such, the literature dealing with it is enormous and spans almost one century of research. Due to the impact on scientific and engineering communities, it is essential to mention the pioneering work of Saville (1955) and the first design curves for irregular waves developed by Goda et al. (1975); in addition, the experimental works of Owen (1980) and van der Meer and Janssen (1994) led to engineering formulae that can be seen as the template for modern overtopping prediction.

As with many other aspects of engineering and science, the transition from the 1900s to the new millennium imparted novel momentum to research and indicated new paths. The process of development began with the EU-funded project *CLASH* (Crest Level Assessment of Coastal Structures by Full-scale Monitoring, Neural Network Prediction and Hazard Analysis on Permissible Wave Overtopping) and has continued to the latest version of the EurOtop Manual (2018), which guides engineers in many scenarios of practical interest.

Altogether, the most forceful elements of novelty of the last 25 years can be summarized as follows:

* Corresponding author.
E-mail address: buccino@unina.it (M. Buccino).

https://doi.org/10.1016/j.oceaneng.2023.116144
Received 31 July 2023; Received in revised form 18 September 2023; Accepted 21 October 2023
Available online 31 October 2023

1) Traditional regression formulae based on the analysis of laboratory outcomes (e.g., Franco et al., 1994; Franco and Franco, 1999; Bruce et al., 2009; Goda, 2009) were joined by new, conceptually different predictive tools. These include Artificial Neural Networks (ANNs), which exploit the availability of large databases (van Gent et al., 2007; Zanuttigh et al., 2016; den Bieman et al., 2021; Habib et al., 2023), and Phase Resolving (PR) numerical models with different levels of complexity, such as Navier-Stokes solvers (CFD, SPH; e.g., Akbari, 2017; Sasani-Babak and Akbari, 2019) and models based on the long wave approximation (shallow water equations, non-hydrostatic models, Boussinesq wave).
2) Besides the mean overtopping rate, further details of the process were investigated, such as the distribution of the individual overtopping volumes (Franco et al., 1994; Besley, 1999; Victor et al., 2012; Nørgaard et al., 2014; Mares-Nasarre et al., 2020; Salauddin et al., 2020, 2022; Koosheh et al., 2021), and the thickness and velocity of the overtopping flow (Schüttrumpf and Van Gent, 2003; Nørgaard et al., 2013; Sandoval and Bruce, 2017; Mares-Nasarre et al., 2019; Altomare et al., 2020; Van der Meer et al., 2022). Moreover, many authors have investigated the effect of modifying the structures' outer profile, e.g., the use of retrofit sea defenses at vertical walls (Pearson et al., 2004; Van Doorslaer et al., 2015; Abolfathi et al., 2018; O'Sullivan et al., 2020; Dong et al., 2020; Dong et al., 2021a,b; Formentin et al., 2021)
3) It was agreed that the wave quantities that control the overtopping process are essentially the moments of order −1 and 0 of the Power Spectral Density (PSD) at the location of the structures. The moments are used to calculate the spectral significant wave height $H_{m0} = 4\sqrt{m_0}$ and the harmonic mean period $T_{m-10} = m_{-1}/m_0$. van Gent (1999) first came to this conclusion, based on the analysis of wave run up and overtopping at impermeable sloping dikes.

Remarkably, the dependence on spectral moments makes the use of PRs almost indispensable when the structure is in the surf zone, as the occurrence of the so-called "surf beats" (Tucker, 1950) carries considerable energy below the peak of the incoming seas (Symonds et al., 1982; Schäffer and Svendsen, 1988; Schäffer, 1993; Henderson and Bowen, 2002), and strongly affects m_{-1} and m_0. As "surf-beats" are dominantly forced by the fluctuation of the breakpoint from wave to wave, they are generally not accounted for in the phase-averaged models, e.g., "SWAN, although interesting developments have been recently discussed in Reniers and Zijlema (2022).

Therefore, as suggested by EurOtop (2018), either phase-resolving models are used to achieve the spectral moments, and then an empirical predictor is applied, or they are employed to calculate the overtopping rate directly. The only alternative to this approach is using empirical formulae that incorporate the effects of surf beats implicitly; however, either these tools require a smoothly varying topography (Hofland et al., 2017; Lashley et al., 2021, 2023) or they are affected by significant uncertainties (Mase et al., 2013).

Hence, we recognize that the rigorous assessment of the performance of phase-resolving models in the surf zone is an urgent need for engineering purposes, either regarding wave overtopping or spectral evolution. However, the body of literature available so far (Aggarwal et al., 2020; Altomare et al., 2021; Lashley et al., 2020; Suzuki et al., 2011; Suzuki et al., 2014; Suzuki et al., 2017; Torres-Freyermuth et al., 2007,

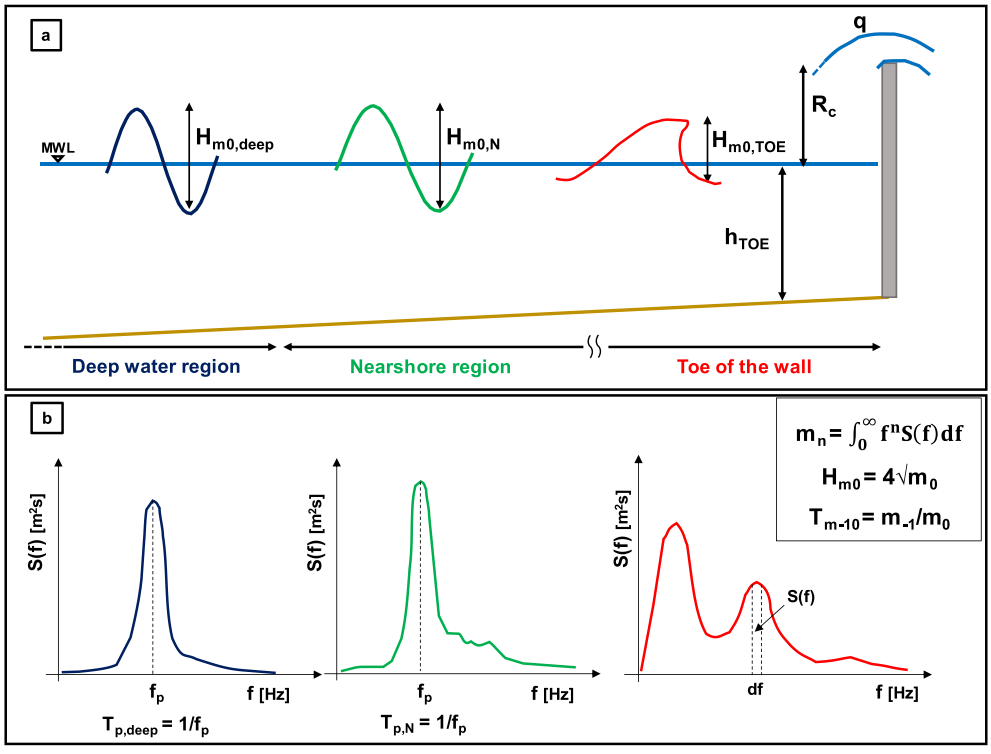

Fig. 1. Sketch of wave evolution and wave overtopping of a vertical seawall. a) definition of geometric and wave characteristics involved in the overtopping process; b) wave spectra in deep water (blue), in the nearshore (green) and in the surf zone (red) as well as the main spectral parameters. E(t), nearshore wave envelope [m]; $E_{RMS\text{-}N,}$ nearshore root mean square envelope of wave elevation signal [m]; f, frequency [Hz]; $f_{p,}$ peak frequency [Hz]; g, gravitational acceleration [m/s^2]; $h_{TOE,}$ still water depth at the toe of the structure [m]; h*, impulsive waves parameter [-]; $H_{m0,deep,}$ deep water spectral wave height [m]; $H_{m0,N,}$ nearshore spectral wave height [m]; $H_{m0,TOE,}$ spectral wave height at the location of the structure [m]; $L_{m\text{-}10,TOE,}$ spectral wave length = $gT_{m\text{-}10,TOE}/2\pi$ [m]; $m_{n,}$ nth order spectral oment [m^2/s^n]; $m_{nB,\ TOE;}$ nth order spectral moment of a linear breaker [m^2/s^n]; $m_{n,\ TOE,}$ nth order spectral moment at the toe of the structure [m^2/s^n]; $m'_{n,\ TOE,}$ non dimensional nth order spectral moment at the toe of the structure [-]; q, mean overtopping discharge per unit crest width [m^3/s/m]; $R_{c,}$ crest freeboard [m]; S(f), power spectral density [m^{2}s]; $T_{m\text{-}10,}$ spectral wave period, based on m_0 and m_{-1} [s]; $T_{p,deep,}$ deep water peak period [s]; $T_{p,N,}$ nearshore peak period [s]; $T_{01,}$ spectral wave period, based on m_0 and m_1 [s]; Δx, horizontal grid dimension [m]; Δz, vertical grid dimension [m]; $\gamma_{b,}$ breaker index [-]; ν, Manning coefficient [m$^{-1/3}$s].

2010) is surprisingly narrow, and exhibits two main flows:

a) No research addressed the case of a rapidly changing foreshore, for which the empirical formulae are unusable.
b) Apart from Lashley et al. (2020), who discussed the results of only two experiments, no systematic comparison has been carried out between models with different degrees of complexity. This point is of particular interest in practical applications, as it indicates the possible trade-offs between the accuracy of the results and the computational times.

This article contributes to filling these gaps by discussing the case of the *Malecòn Tradicional* Seawall of La Habana (Cuba), a vertical wall that has protected the city's most historic neighborhoods since the late 1800s; it rests on less than 2.0 m water depth and is affected by a steeper and more irregular foreshore than those studied so far.

Laboratory experiments at the University of Napoli Federico II are replicated using two computationally different numerical approaches: CFD-RANS and the non-hydrostatic model SWASH based on the Nonlinear Shallow Water Equations. Both numerical and physical model tests were preliminarily carried out in the absence of the structure, allowing an in-depth wave propagation analysis.

However, the work is not limited to a mere comparison of the results; instead, it interprets the data from the perspective of gaining a deeper insight into the physics of the phenomena and sheds some light on the most efficient hydraulic quantities that control the overtopping process in a surf zone. In this view, particular attention is paid to the relationship between spectral moments and overtopping rate, for which, as will be shown, there are still some uncertainties.

The article is organized as follows. Sections 2 describes the laboratory and numerical studies, highlighting their respective peculiarities. Results on wave evolution are discussed in Sections 3.1 and 3.2, while 3.3 deals with the analysis of wave overtopping.

2. Materials and methods

2.1. The Malecòn Tradicionàl (MT) laboratory experiments

2.1.1. Overview of the experimental campaign

2D laboratory experiments were carried out at the University of Naples "Federico II" (Italy) to pinpoint possible variants of the Malecòn Traditionàl, which would mitigate the severe flooding events periodically experienced by the back districts (Còrdova Lopez et al., 2015; 2016).

The experimental campaign was conducted at a scale of 1:30 in a flume 18.4 m long and 1.55 m wide; the device is equipped with a piston-type wavemaker, with a 0.25 m maximum semi-stroke, and an active absorption system based on a dual signal control algorithm in the frequency domain (Schaffer and Jakobsen, 2003; HR Wallingford, 2005).

The underwater beach was modeled from the location of the MT, which is 1.70 m below the Mean Water Level (MWL), out to a depth of 18.72 m; farther towards the wavemaker, the bottom is flat to allow the generated waves to develop appropriately (Fig. 2).

The tests were performed with two water levels, namely +1.73 m and +2.28 m at the prototype scale (+0.06 m and +0.076 m in the model); they correspond respectively to the 50 years return period sea level rise (including astronomical tide, storm surge, and climate change effects) and the surge observed during the hurricane Wilma occurred in 2005. For each level, eight sea states driven by mean JONSWAP spectra were generated, which are representative of the extreme Cuban climate; in particular, four values of the significant wave height were used (2.5 m, 4.0 m, 5.4 m, and 6.5 m), with two peak periods (10s and 12s).

To assess the incoming wave conditions at the toe of the wall ("*TOE*" waves), the sea-states were run on the seabed for 200 waves; this also allowed the calibration of the incident wave conditions on the flat bottom that precedes the foreshore, which we will refer to as the "*Nearshore zone*" as the ratio $\tanh kh/kh$ (for the peak-period) is about 0.9. The "*Nearshore waves" were estimated* by applying the separation method of Zelt and Skjelbreia (1992) to an array of four probes, according to Fig. 2. As widely known, this separation technique is based on a frequency domain least square approach, which uses weighting coefficients to enhance the accuracy of the results. All the wave gauges were sampled at 25 Hz.

Subsequently, the mean overtopping rate was estimated on a sequence of 1000 waves with the structure in place. The overtopping water was collected in a trail and then recirculated using two submersible pumps with an overall capacity of 800 l/min. The pumped water passed through an electromagnetic flow meter, which computed the fluid volume progressively. The water level in the reservoir at the beginning and at the end of each test was controlled by a supplementary wave probe.

Meanwhile, an array of four pressure transducers, sampled at 2500 Hz, measured the wave loadings along the wall. As shown in Fig. 3, the waves induce severe impulsive pressures onto the structure, reaching 60 times the local significant wave height.

This article deals with only 48 of the 360 experiments in the MT campaign. These tests were carried out with plain-wall profiles and are therefore referred to as the Plain-Wall Subset (PWS).

PWS tested three heights of the wall at the prototype scale, namely

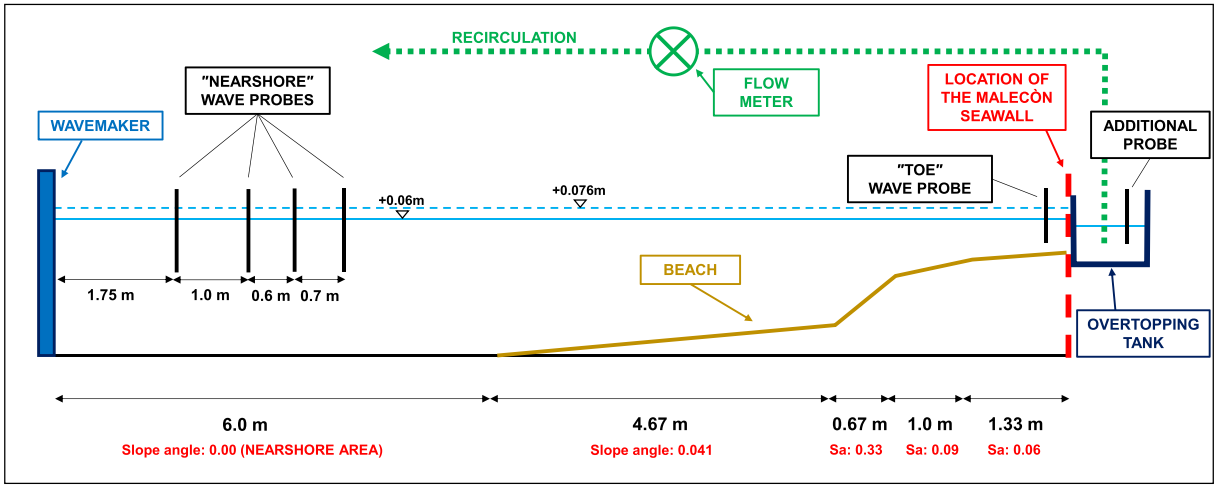

Fig. 2. Sketch of the MT's experimental setup. Dimensions are in the model's scale (1:30).

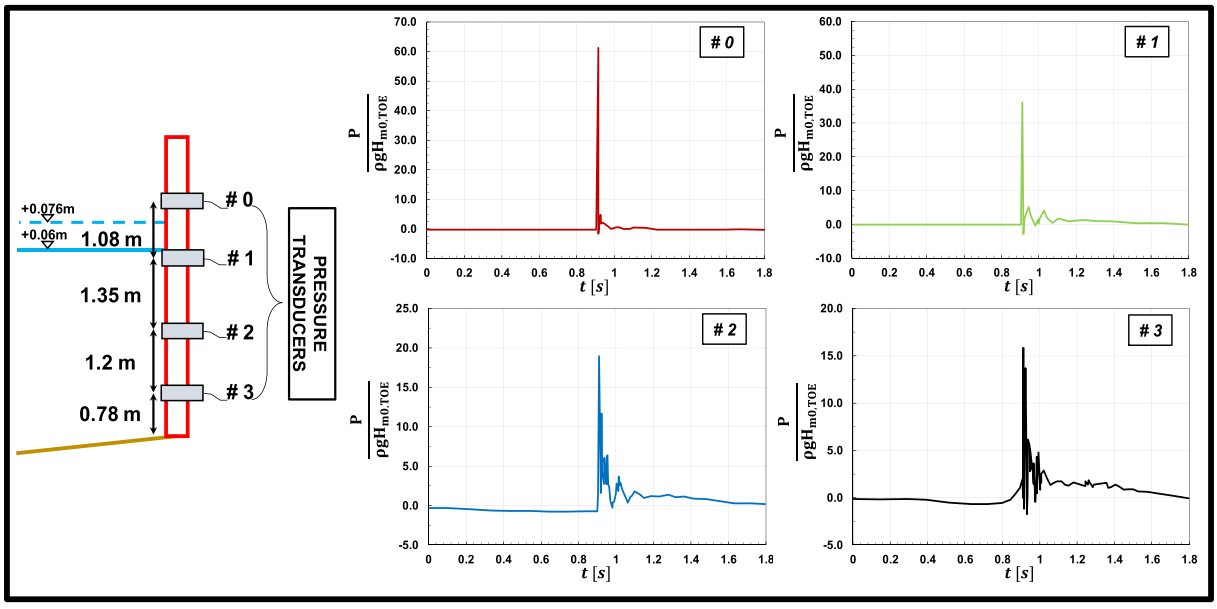

Fig. 3. Example of pressure measurements at the Malecòn. Dimensions are in the model's scale (1:30).

3.96 m above the MWL (original height of MT), 4.46 m, and 4.96 m (prototype scale); in combination with two sea levels, this results in 6 values for the crest freeboard R_c.

2.1.2. The characteristics of the plain wall subset (PWS)

The range of the most relevant hydraulic variables for PWS is reported in Table 1, where the subscripts "*N*" and "*TOE*" denote, respectively, the "*Nearshore*" conditions and the conditions at the location of the structure.

The parameter $h^* = \frac{h_{TOE}^2}{L_{-10,TOE} \bullet H_{m0,TOE}}$ discriminates the loading case at the wall (EurOtop, 2018); values as low as in the table predict the occurrence of severe wave impacts, which is in agreement with the pressure measurements in Fig. 3.

However, the inherent peculiarity of these data emerges clearly from the fact that 35 experiments out of 48 (73%) fall outside the training set boundaries of the EurOtop's Neural Network. The comparison with the EurOtop data in Fig. 4 can help to better understand the reasons for this.

Restricting the analysis to plain walls in "non-deep waters" ($h_{TOE}/H_{m0,deep} \leq 4$; Hofland et al., 2017), the EurOtop data classified as "*Very Reliable*" or "*Reliable*" amount to 150. Of these, only nine fall within the very shallow water domain ($0.3 \leq h_{TOE}/H_{m0,deep} \leq 1$), where PWS counts 36 experiments instead (Fig. 4a). Moreover, these nine data have $h_{TOE}/H_{m0,deep} \geq 0.82$, which indicates that the breaking process is only in the early stages of its development.

These characteristics reverberate in the ratio $T_{p,deep}/T_{m\text{-}10\ TOE}$ pictured in Fig. 4b. In contrast to PWS, which even reaches values below 0.33, all EurOtop data exceed 0.9, which corresponds to waves with no or very few surf beats in the PSD. Therefore, the structure of the EurOtop data does not allow the establishment of a real relationship between the overtopping rate and the low-frequency components of the spectrum, since $T_{m\text{-}10\ TOE}$ does not actually provide any information other than $T_{p,deep}$.

More generally, the behavior of a vertical seawall subject to a large number of broken waves could not be properly assessed.

It is also worth mentioning that the great majority of the data analyzed by Lashley et al. (2021) on vertical seawalls belongs to the "Non-Reliable" part of the EurOtop database; this further renews the interest in the analyses discussed herein.

2.2. Numerical study

The primary purpose of the numerical study is to compare the performance of PR models with different degrees of complexity.

In this view, we employ the CFD-RANS technique and the non-hydrostatic model SWASH based on the Nonlinear Shallow Water Equations. The tests concern only the 1.73 m sea level rise, for which wave breaking is very intense, and the experimental conditions deviate more markedly from those investigated in EurOtop's analysis. The laboratory layout was scaled to the prototype (1:1) to check for possible scale effects in the physical experiments and to analyze the models' behavior under "real-life" dimensions. Thus, all the results discussed from now on refer to the prototype scale.

2.2.1. CFD-RANS experiments

CFD-RANS simulations were carried out with *Flow3D*, a sophisticated and versatile Computational Fluid Dynamics platform developed by Flow Science Inc. (2009). The software was used to integrate the incompressible Reynolds-Averaged Navier-Stokes Equations (RANS) for a single fluid that flows in the x,z vertical plane; the x-axis is directed toward the shore, whereas z points upwards.

The equations for the conservation of mass and momentum then read:

$$\frac{\partial u_x}{\partial x} + \frac{\partial u_z}{\partial z} = 0 \tag{1}$$

Table 1
Characteristics of PWS. The subscript "*N*" denotes the Nearshore wave conditions (prototype scale). Note that $H_{m0,\ deep}$s are calculated from $H_{m0,N}$s via linear deshoaling.

#data	$H_{m0,N}$ [m]	$T_{p,N}$ [s]	$h_{TOE}/H_{m0,deep}$ [-]	h_* [-]	$h_{TOE}/L_{m\text{-}10,TOE}$[-]	$R_c/H_{m0,TOE}$[-]
48	**2.7–6.5**	10 and 12	0.52–1.52	0.003–0.048	0.002–0.030	0.473–1.879

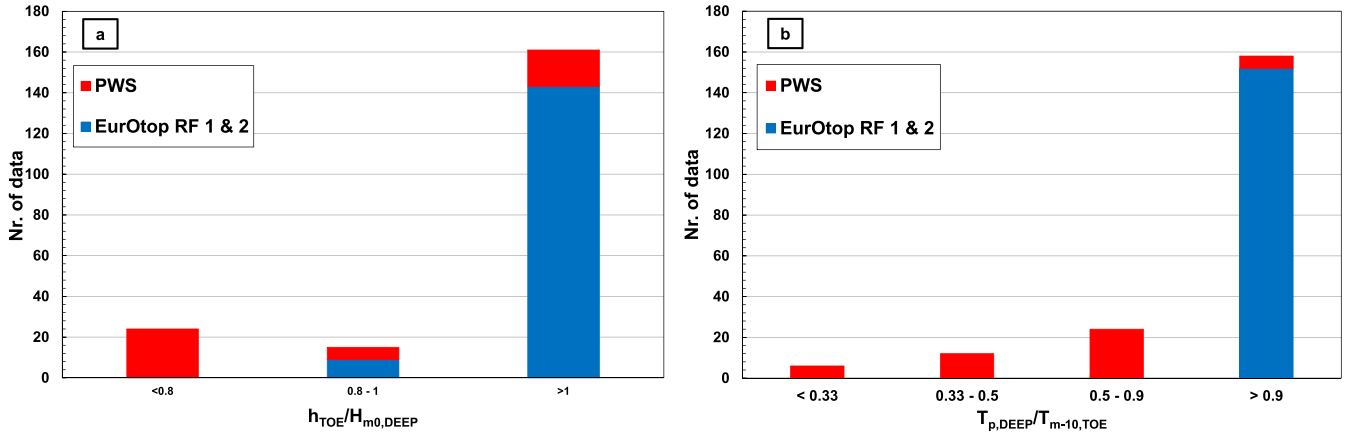

Fig. 4. Comparison between PWS and EurOtop database for plain walls in shallow waters (Reliability Factor = 1 & 2).

$$\frac{\partial u_x}{\partial t}+u_x\frac{\partial u_x}{\partial x}+u_z\frac{\partial u_x}{\partial z}+\frac{1}{\rho}\frac{\partial p}{\partial x}-2\frac{\partial}{\partial x}\left[(\nu+\nu_T)\left(\frac{\partial u_x}{\partial x}\right)\right]-\frac{\partial}{\partial z}\left[(\nu+\nu_T)\left(\frac{\partial u_x}{\partial z}+\frac{\partial u_z}{\partial x}\right)\right]=0 \quad (2)$$

$$\frac{\partial u_z}{\partial t}+u_x\frac{\partial u_z}{\partial x}+u_z\frac{\partial u_z}{\partial z}+g+\frac{1}{\rho}\frac{\partial p}{\partial z}-\frac{\partial}{\partial x}\left[(\nu+\nu_T)\left(\frac{\partial u_x}{\partial z}+\frac{\partial u_z}{\partial x}\right)\right]-2\frac{\partial}{\partial z}\left[(\nu+\nu_T)\left(\frac{\partial u_z}{\partial z}\right)\right]=0 \quad (3)$$

where **u** (u_x; u_z) denotes the turbulence-averaged velocity field, p is the turbulence-averaged pressure, **g** (0;g) is gravity, ρ is the water density, and ν and ν_T indicate, respectively, kinematic and eddy viscosity.

To calculate ν_T, two additional transport equations must be solved, which express the balance of the turbulent kinetic energy, k, and the dissipation rate, ε:

$$\frac{\partial k}{\partial t}+u_x\frac{\partial k}{\partial x}+u_z\frac{\partial k}{\partial z}-\frac{\partial}{\partial x}\left[\frac{(\nu+\nu_T)}{\sigma_k}\left(\frac{\partial k}{\partial x}\right)\right]-\frac{\partial}{\partial z}\left[\frac{(\nu+\nu_T)}{\sigma_k}\left(\frac{\partial k}{\partial z}\right)\right]+\epsilon-P=0 \quad (4)$$

$$\frac{\partial \epsilon}{\partial t}+u_x\frac{\partial \epsilon}{\partial x}+u_z\frac{\partial \epsilon}{\partial z}-\frac{\partial}{\partial x}\left[\frac{(\nu+\nu_T)}{\sigma_\epsilon}\left(\frac{\partial \epsilon}{\partial x}\right)\right]-\frac{\partial}{\partial z}\left[\frac{(\nu+\nu_T)}{\sigma_\epsilon}\left(\frac{\partial \epsilon}{\partial z}\right)\right]+c_2\frac{\epsilon^2}{k}-c_1\frac{\epsilon}{k}\nu_T P=0 \quad (5)$$

In the equations above, P is the shear production:

$$P=\frac{(\nu+\nu_T)}{\rho}\bullet\left[2\left(\frac{\partial u_x}{\partial x}\right)^2+\left(\frac{\partial u_x}{\partial z}+\frac{\partial u_z}{\partial x}\right)^2+2\left(\frac{\partial u_z}{\partial z}\right)^2\right] \quad (6)$$

whereas σ_k, σ_ε, c_1 and c_2 are specific coefficients.

In this work, we assume σ_k, σ_ε, and c_1 to be constant, whereas c_2 is allowed to vary in the function of P,k, and ε (Yakhot and Smith 1992). This results in the well-known ReNormalized Group (RNG) extension of the standard κ−ε turbulence closure, which Bradford (2000) reasoned to be particularly suited to steep foreshores affected by plunging breakers (see also Bahmanpouri et al., 2021). Moreover, Buccino et al. (2019a,b) have used it in the analysis of an overtopped caisson breakwater, finding a good agreement with the measurements of Walkden et al. (2001).

Fig. 5 gives a sketch of the numerical flume and summarizes the boundary conditions (BCs) employed.

At the end of the channel opposite the Wave generation, two different BCs are used: in the presence of the wall, the "*Outflow condition*" allows the waves to leave the domain without any reflections. Otherwise, without structure, "*Pressure*" guarantees a constant water level.

The lateral and upper bounds of the computational domain are treated as "*Symmetry boundaries*" where the velocity gradient vanishes, and turbulence production is zero. Finally, a "*Wall*" condition is imposed at the bottom, which cancels out the velocity component normal to the seafloor.

Wave generation exploits the mass source concept introduced by Lin and Liu (1999), which adds a source term to the continuity eq. (1). As shown in Fig. 5, the sea-states are generated by an underwater parallelepiped, through which the fluid enters the computational domain at a desired speed.

This generation technique also allows adding a wave-damping zone at the beginning of the flume, which functions as an active absorption system. Based on preliminary tests, we fixed the length of the damping zone at 100 m, with a 0.5 m × 1.0 m x 0.5 m internal mesh. The damping

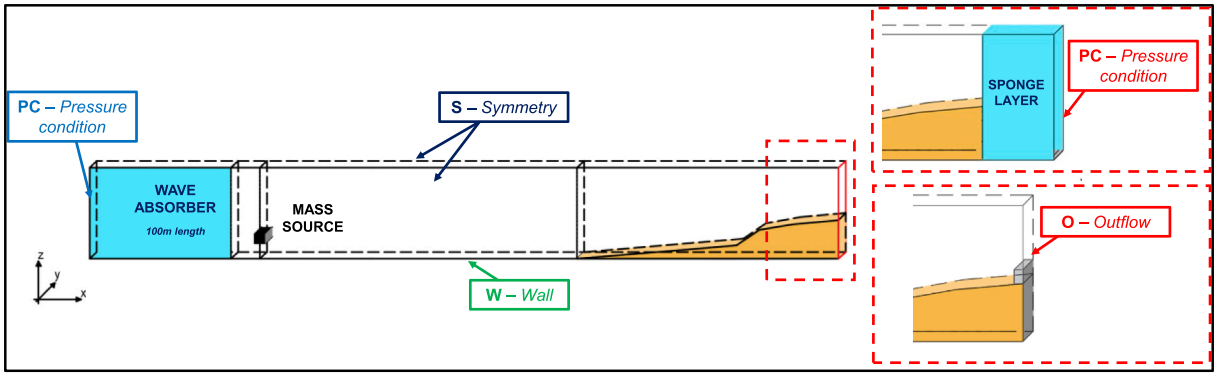

Fig. 5. BCs employed in the CFD-RANS model.

coefficient varied linearly from 0 to 1 (Wei, 2015).

It is worth noting that the occurrence of breaking, along with the significant amount of overtopping water, reduced the rate of reflection considerably, which enabled the reduction of the length of the adsorber, and the use of a steeper damping function compared to other CFD studies (e.g., the logarithmic function adopted in Akbari and Pooyarad, 2020).

After considering eight mesh layouts (Appendix A.1.1), the flow domain was finally discretized into 272,275 rectangular cells. From the wave generation up to 100 m from the wall, the cells have $\Delta x = 0.70$ m and $\Delta z = 0.30$ m, whereas in the rest of the computational domain, the dimensions reduce to $\Delta x = 0.40$ m and $\Delta z = 0.15$ m. This allowed it to save computational time (reducing the number of cells) while maintaining adequate vertical resolution both in the innermost surf zone and along the structure.

Flow3D solves the set of PDEs that govern the problem according to a staggered grid finite difference scheme, while the free surface is tracked according to the Volume of Fluid (VOF) technique (Hirt and Nichols, 1981). The software adopts a variable time step to maintain the stability and accuracy of the solution, which satisfies the Courant–Friedrichs–Lewy (CFL) stability criterion and ensures that surface waves cannot propagate more than one cell per time step.

As shown in Table 2, 37 random wave experiments were carried out, lasting between 200 and 500 waves. To the authors' knowledge, this is the widest array of CFD tests published so far concerning a surf zone.

However, it should be highlighted that despite the same spectrum shape, the "*Nearshore*" waves generated with *Flow3D* differ from those of the physical model by the values $H_{m0,N}$ and in terms of time-domain properties.

As shown in Fig. 6, while the laboratory waves remain approximately Gaussian even for the largest values of *the* wave height (panels a and c), CFD waves become positively skewed (panels b and d), with the crests being increasingly higher than troughs.

Since wave skewness plays a role in the breaking process, such a peculiarity must be properly accounted for in the analysis of results. On the other hand, the macrofeatures of surf zone, which is dominated by plunging breakers, are reproduced realistically (not shown for brevity).

It is finally worth highlighting that the large-scale modelling, together with the limited extent of the shoal, prevented the waves from decaying anomalously due to the overproduction of turbulent energy, as described in Larsen and Fuhram (2018) and Li et al. (2022). For an example, see Figure A.1.2 of Appendix A.1.

2.2.2. SWASH

SWASH (Acronym for Simulating WAves till SHore) is an increasingly popular wave flow model that extends the Non-Linear Shallow Water Equations (NLSW) with a non-hydrostatic pressure term and a simplified momentum balance in the vertical direction (Zijlema et al., 2011). It is based on an explicit second-order finite method for staggered grids and a second-order leapfrog scheme for time integration (Hansen, 1956), which make it particularly suitable for simulating shallow water phenomena; these include wave breaking, bore propagation (Toro, 2001; Smit et al., 2013), generation of surf-beats, wave runup, and wave overtopping (Suzuki et al., 2017). Furthermore, the dispersive properties of gravity waves are efficiently accounted for by dividing the computational domain into a fixed number of terrain-following layers (Zijlema and Stelling, 2005, 2008).

The depth-integrated non-hydrostatic flow is described by the following equations:

$$\frac{\partial \zeta}{\partial t} + \frac{\partial (h+\zeta) U_X}{\partial x} = 0 \tag{7}$$

$$\frac{\partial U_X}{\partial t} + U_X \frac{\partial U_X}{\partial x} + g \frac{\partial \zeta}{\partial x} + \frac{1}{2} \bullet \frac{\partial p_b}{\partial x} + \frac{p_b}{2 \bullet (h+\zeta)} \frac{\partial (\zeta - h)}{\partial x} + c_f \frac{U_X \bullet |U_X|}{(h+\zeta)} = 0 \tag{8}$$

$$\frac{\partial \left(u_{z,s} - u_{z,b}\right)}{\partial t} - \frac{2 p_b}{(h+\zeta)} = 0 \tag{9}$$

$$u_{z,b} + \frac{\partial (h+\zeta) U_X}{\partial x} = 0 \tag{10}$$

$$\frac{\partial U_{x.}}{\partial x} + \frac{u_{z,s} - u_{z,b}}{(h+\zeta)} = 0 \tag{11}$$

in which ζ (x,t) is the free surface, $h(x)$ is the geometric water depth, U_X (x,t) is the depth-averaged horizontal velocity, p_b(x,t) is the non-hydrostatic pressure at the bottom (divided by density), and $u_{z,s}$ and $u_{z,b}$ denote vertical velocities at the free surface and bottom respectively. Finally, c_f is the non-dimensional friction parameter, which is calculated from the Manning coefficient, ν.

Eqs. (7) and (11) express global and local conservation of mass, while Eq. (8) is the depth-averaged momentum balance along the x direction. The momentum equation for $u_{z,s}$ is given by Eq. (9), which includes only the inertial terms, whereas Eq. (10) is the kinematic bottom condition, enabling us to calculate $u_{z,b}$.

SWASH significantly reduces the computational efforts compared to CFD-RANS since NLSW permit the tracking of the free surface using a single-valued function of the horizontal coordinates only (unlike VOF); moreover, it requires a low vertical resolution to achieve accurate results (1 or 2 terrain layers), as shown in Zijlema and Stelling (2005, 2008).

The experiments discussed in this study replicate the PWS tests with a sea level rise of 1.73 m; accordingly, they include eight propagation experiments on the shoal, which lasted 200 waves, and 24 overtopping tests with a duration of 500 waves.

At the generation boundary, the same "*Nearshore*" wave elevation time-series were imposed as the laboratory experiments, so that numerical and physical sea states match in both the time and frequency domains (Fig. 7). Conversely, at the opposite end of the channel a Sommerfield BC was used to minimize wave reflection. The wave breaking has been modeled via the HFA method developed by Smit et al. (2013).

The water depth was divided into 2 layers, and the maximum Courant number was set at 0.5. After the sensitivity analysis discussed in Appendix A.1.2, we selected a grid spacing of 1 m and a Manning coefficient of zero.

3. Results

The performance assessment of numerical models with different degrees of complexity, such as SWASH and CFD-RANS, will certainly be an important subject of the sections below. Nevertheless, the analysis also attempts to point out some aspects of the physics of the investigated processes, which may have an impact on engineering applications.

In the pursuit of this dual objective, Sections 3.1 and 3.2 deal with the evolution of waves in the absence of structure and focus on PSD and

Table 2
Nearshore wave parameters for CFD-RANS experiments. $H_{m0,N}$ are calculated according to Zelt and Skjelbreia (1992).

TYPE	WAVE SPECTRUM	#test	duration (#waves)	$H_{m0,N}$ [m]	$T_{p,N}$ [s]	Wall height in m above MWL
Propagation	***JONSWAP***	10	200	1.35–6.43	10–12	No wall
Overtopping	***JONSWAP***	27	500	2.88–6.43	10–12	3.96, 4.46, 4.96 m

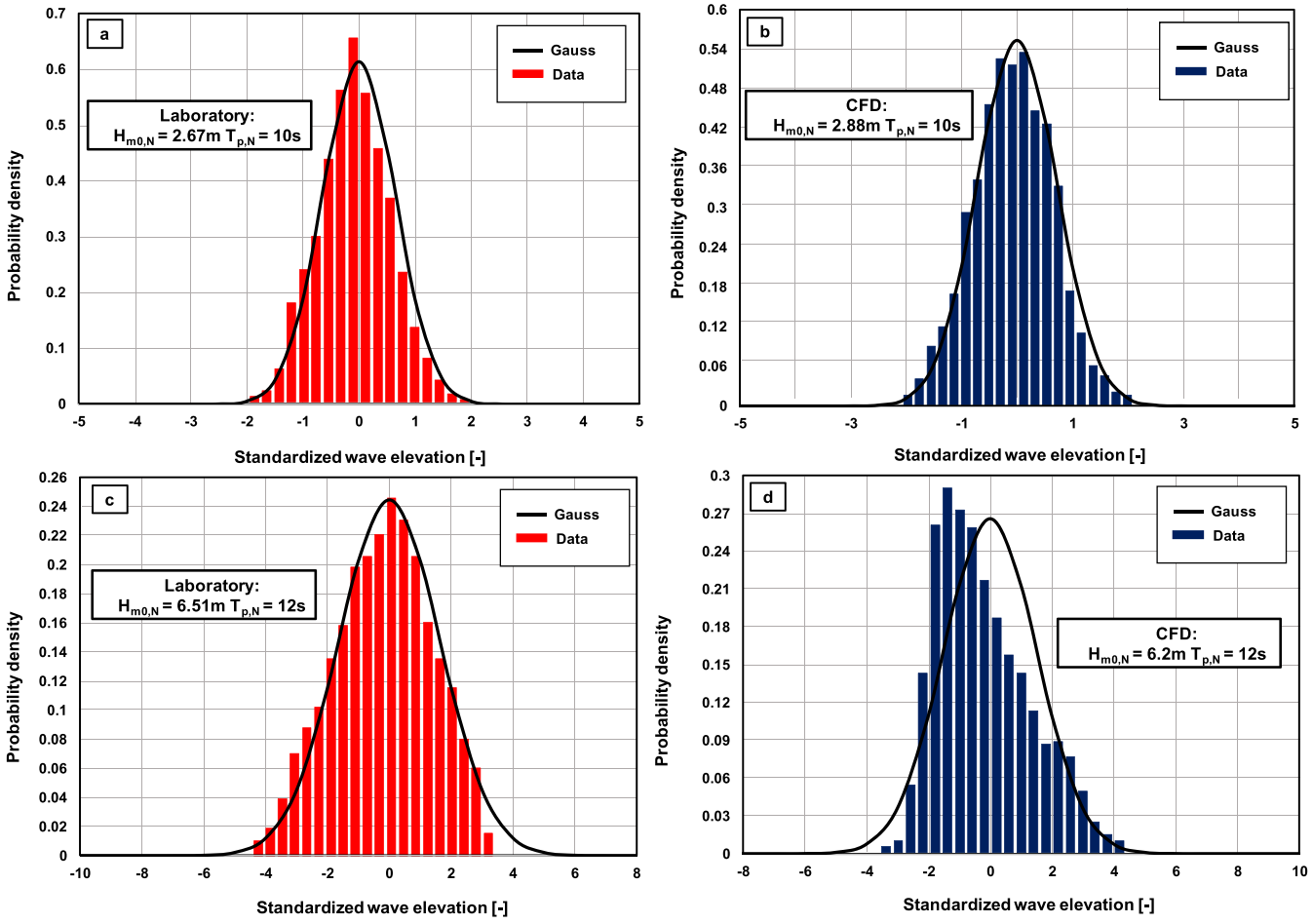

Fig. 6. Distribution of laboratory and CFD surface elevation (standardized) in the "Nearshore" zone.

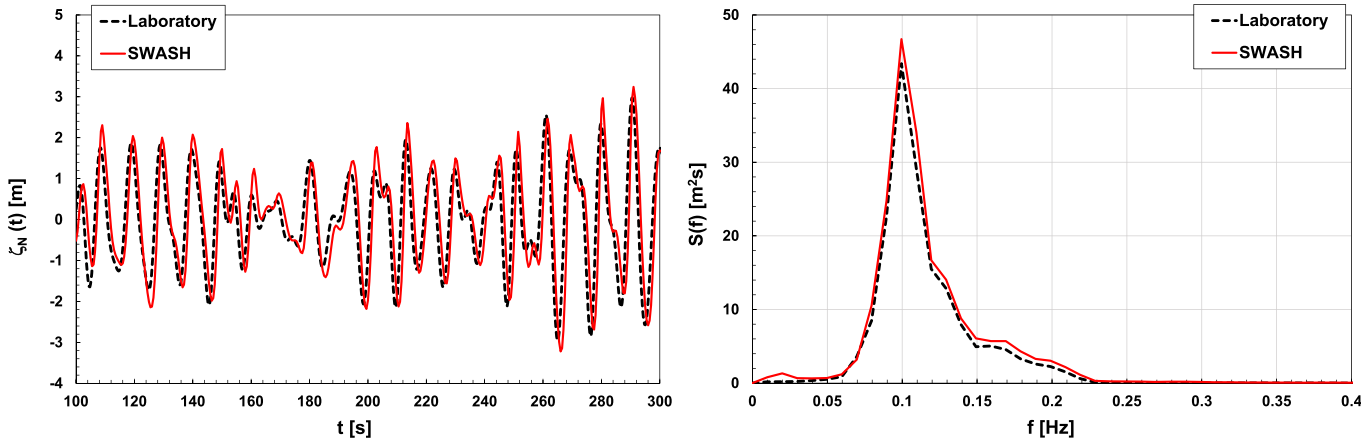

Fig. 7. Laboratory vs SWASH surface elevation time-series (left panel) and PSD (right panel). $H_{m0,N}$ = 5.4 m, $T_{p,N}$ = 10s.

wave setup respectively. The overtopping discharge is then analyzed in Section 3.3.

3.1. Analysis of the spectral evolution (PSD)

Recent research by Hofland et al. (2017) and Lashley et al. (2021) on planar beaches have indicated that spectral quantities in the surf zone, such as H_{m0} and T_{m-10}, can be efficiently predicted from the corresponding deep water values $H_{m0,deep}$ and $T_{m-10,\ deep}$. Following Goda (1975, 2000), the authors used the wave height to depth ratio ($H_{m0,deep}/h$) and the offshore mean wave steepness (s_{m-10}) as the main predictor variables.

In this section, we generalize the approach and address the relationships between the properties of the "*Nearshore*" waves and the spectral moments at the toe of the wall , $m_{n,TOE}$.

In this view, to account for the skewness of the RANS wave elevation

chronograms shown Fig. 6, we characterize the "*Nearshore*" waves in terms of their envelope function *E(t),* which we obtain via Hilbert transform of the wave oscillation signals (Fig. 8).

Wave height to depth ratio and wave steepness are thus replaced by the following quantities:

$$r_E = \frac{E_{rms-N}}{h_{TOE}} \tag{12}$$

$$s_{E,P} = 2\pi \bullet \frac{E_{rms-N}}{gT_{PN}^2} \tag{13}$$

in which E_{rms-N} denotes the effective envelope value; as widely known, $E_{rms-N} = \sqrt{2 \bullet m_{0,N}} = \frac{1}{2} \bullet H_{rms}$ for symmetric Gaussian wave processes (Tayfun and Lo, 1989), and increases as the wave profile becomes skewed.

A further advantage of using the effective envelope is that in virtue of the equality:

$$[E_{rms-N}]^2 = [Mean\ E(t)]^2 + VAR\ E(t) \tag{14}$$

it is explicitly linked to the variance of *E(t),* and then to the modulation of the envelope. The latter is in turn closely related to the generation of surf-beats, as these long waves are primarily forced by the fluctuation of the breaking point from wave to wave (Symonds et al., 1982).

3.1.1. Malecòn results and comparison with numerical models

Fig. 9 shows the results of the laboratory and numerical *Malecòn* experiments concerning the spectral moments of orders *n = -1, 0, 1 and 2*.

The ordinates of the graph plot the ratio*:*

$$m'_{n,TOE} = \frac{m_{n,TOE}}{m_{nB,TOE}} \tag{15}$$

where the quantity:

$$m_{nB,TOE} = \frac{1}{2}\gamma_b^2 h_{TOE}^2 (T_{p,N})^{-n} \tag{16}$$

represents the nth moment of a linear (narrow band) breaker with amplitude $a_B = \gamma_b h_{TOE}$. According to Kamphuis (1996), an order of magnitude value $\gamma_b = 0.3$ is adopted hereafter, corresponding to a wave height to depth ratio of 0.6 (see also Kamphuis, 1991).

The abscissas report instead the set of empirical predictors:

$$x_n = \left(\frac{E_{rms-N}}{h_{TOE}}\right)^2 \bullet [s_{E,P}]^{-\frac{n+1}{2}} \tag{17}$$

which combine the variables (12) and (13). In Eq. (17), $\left(\frac{E_{rms-N}}{h_{TOE}}\right)^2$ roughly represents the excess wave energy propagating from the Nearshore zone, while $[s_{E,P}]^{-\frac{n+1}{2}}$ is a weighting function that accounts for the fact that dissipation by breaking is more intense for steep waves (e.g., Battjes and Janssen, 1978). As the breaking process has a greater influence on the high frequencies of the spectrum, the exponent of $s_{E,P}$ increases with the moment order *n*.

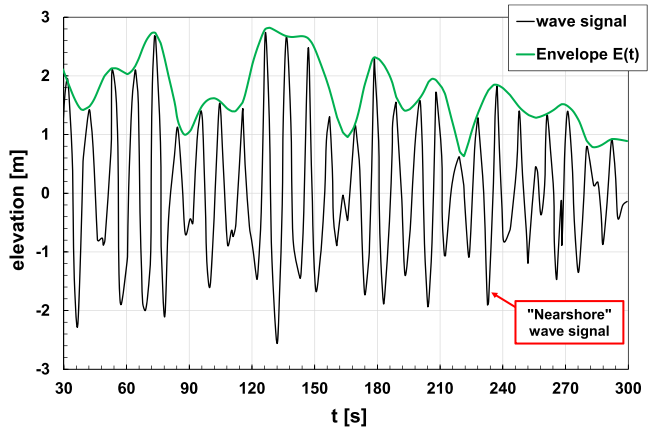

Fig. 8. Envelope of the Nearshore waves.

In Fig. 9, it can be seen that both numerical and laboratory $m'_{n,TOE}$s increase almost linearly with the respective abscissas.

For the −1 moment, which depends primarily on the low-frequency spectral components, the increase is due to the generation of surf-beats as the Nearshore envelope grows high; on the other hand, the trends of $m'_{1,TOE}$ and $m'_{2,TOE}$ indicate that the steep foreshore does not allow the breakers to dissipate all the excess shortwave energy.

According to the saturated breakers theory by Le Mehaute (1962), this is because when the water depth changes rapidly, the demand for energy dissipation increases too fast compared to the damping capacity of the breakers. Thus, as the Nearshore climate becomes more intense, all the spectral components keep on increasing, and no "depth-controlled" condition is reached.

The numerical models properly reproduce the qualitative trends of the laboratory data. However, while RANS experiments keep reasonably close to the physical model, SWASH overpredicts all the spectral moments apart from $m'_{-1,TOE}$. Therefore, it underestimates the dissipation of energy in the high frequency range, including around $T_{p,N}$, but correctly simulates the generation of surf-beats.

The behavior of the software can be more intuitively compared in Fig. 10, which shows the PSDs at the toe of the wall for two experiments with the same values of E_{rms-N} and $T_{p,N}$.

It is worth to notice that RANS experiments also tend to overestimate the higher order moments of the spectrum, particularly $m'_{2,TOE}$ (panel d in Fig. 9); accordingly, the dampening of the superharmonics in the surf-zone is weaker than in the lab, as can be observed in the high frequency range of Fig. 10.

As this phenomenon proved independent of the turbulence model (not shown here), it may be due to either the "Wall" (slip) condition imposed at the bottom, which affects the boundary layer in the numerical flume, or to a viscosity-related scale effect in the physical model, which augments dissipation.

3.1.2. Comparison with a mild surf-zone

The results of Fig. 9 can be provided with a more robust physical meaning if compared with the behavior of a gentle beach. To this end, Fig. 11 shows the results of the laboratory experiments of van Gent (1999), carried out on a slope inclined 1/100 to the horizontal.

The clearest difference with Fig. 9 is that both the zeroth and first moment of the shallow water spectra tend towards a constant "depth-controlled" value of the order of 0.8; indeed, due to the small beach angle, the dissipation demand increases now only slowly, and the breakers can dissipate almost all the energy surplus coming from offshore.

On the other hand, $m'_{-1,TOE}$ still exhibits a linear trend, as surf beats are almost unaffected by breaking; the increment rate is nearly half that for Malecòn, just because the damping of the high-frequency components is more intense.

3.1.3. Spectral moments and engineering predictors

The trends observed above lead to interesting consequences on the correlation between the spectral moments, a feature to which coastal engineers generally pay little attention.

As is widely known, ocean wave spectra in deep and shoaling waters are confined to a narrow band of energy, and therefore, they have moments that are simply proportional to each other; accordingly, mean spectral periods such as T_{m-10} and T_{01} are functions solely of T_p, and are independent, at least theoretically, of the wave energy.

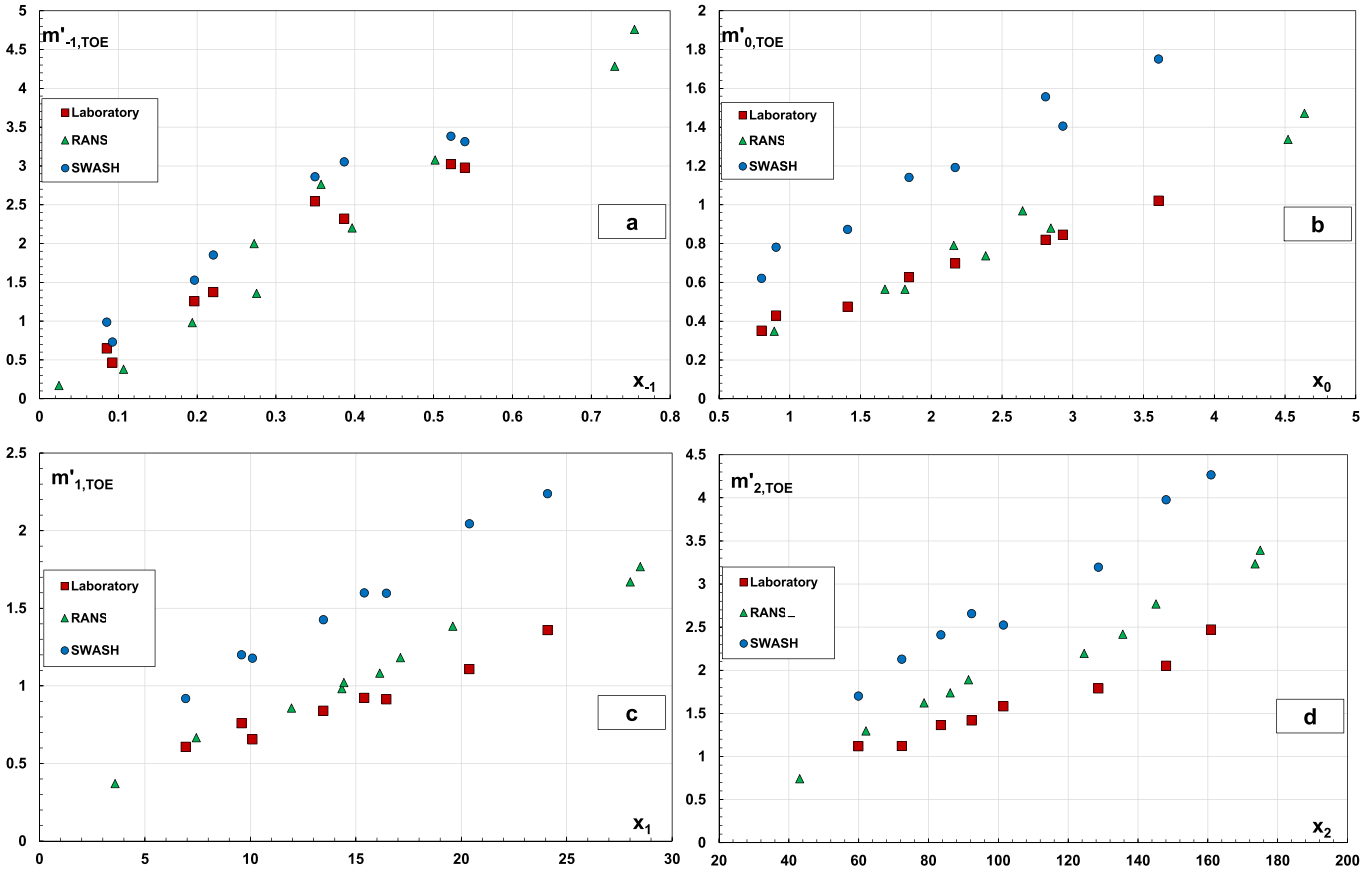

Fig. 9. Non dimensional spectral moments in the function of x_n.

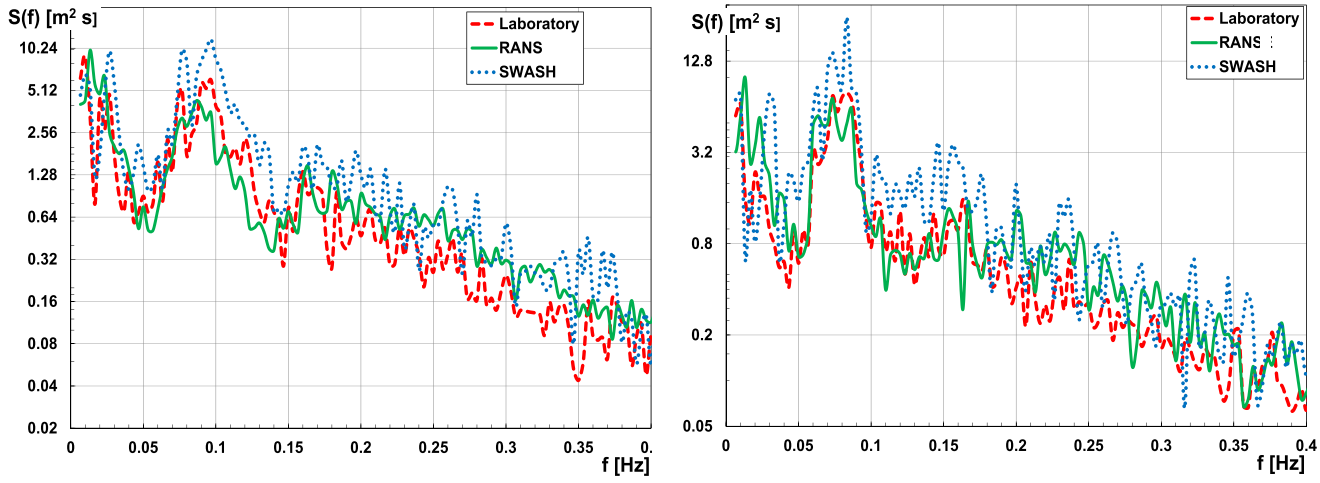

Fig. 10. Laboratory vs. numerical wave spectra at the toe of the wall. Left panel: $E_{rms-N} = 2.48m$, $T_{p,N} = 10s$. *Right panel* $E_{rms-N} = 2.15m$, $T_{p,N} = 12s$.

An example relative to present data is shown in Fig. 12.

However, the narrow band assumption is no longer appropriate in the surf zone, and therefore, significant relationships will arise between $T_{m-10,TOE}$, $T_{01,TOE}$, and $m_{0,TOE}$.

Figs. 13 and 14 show that as long as the spectral moments increase linearly with the corresponding x_{ns} (like in Figs. 9 and 11a), the correlation degree between wave energy and mean spectral periods remains globally high (R^2 of the order of 0.8/0.9). Conversely, the fact that the first-order moment in Fig. 11c tends to become "depth-controlled" weakens the relationship between m_0 and T_{01} by far ($R^2 = 0.28$ in Fig. 14b).

Hence, we may argue that the local wave energy tends to be correlated with both the mean spectral periods on steep foreshores, while on mild beaches, this is only true of T_{m-10}.

The analysis of these correlation structures is of great interest for engineering purposes, as either the wave energy or the spectral periods are used as predictors in analyzing wave overtopping and other phenomena of practical interest. Ignoring their mutual relationships can,

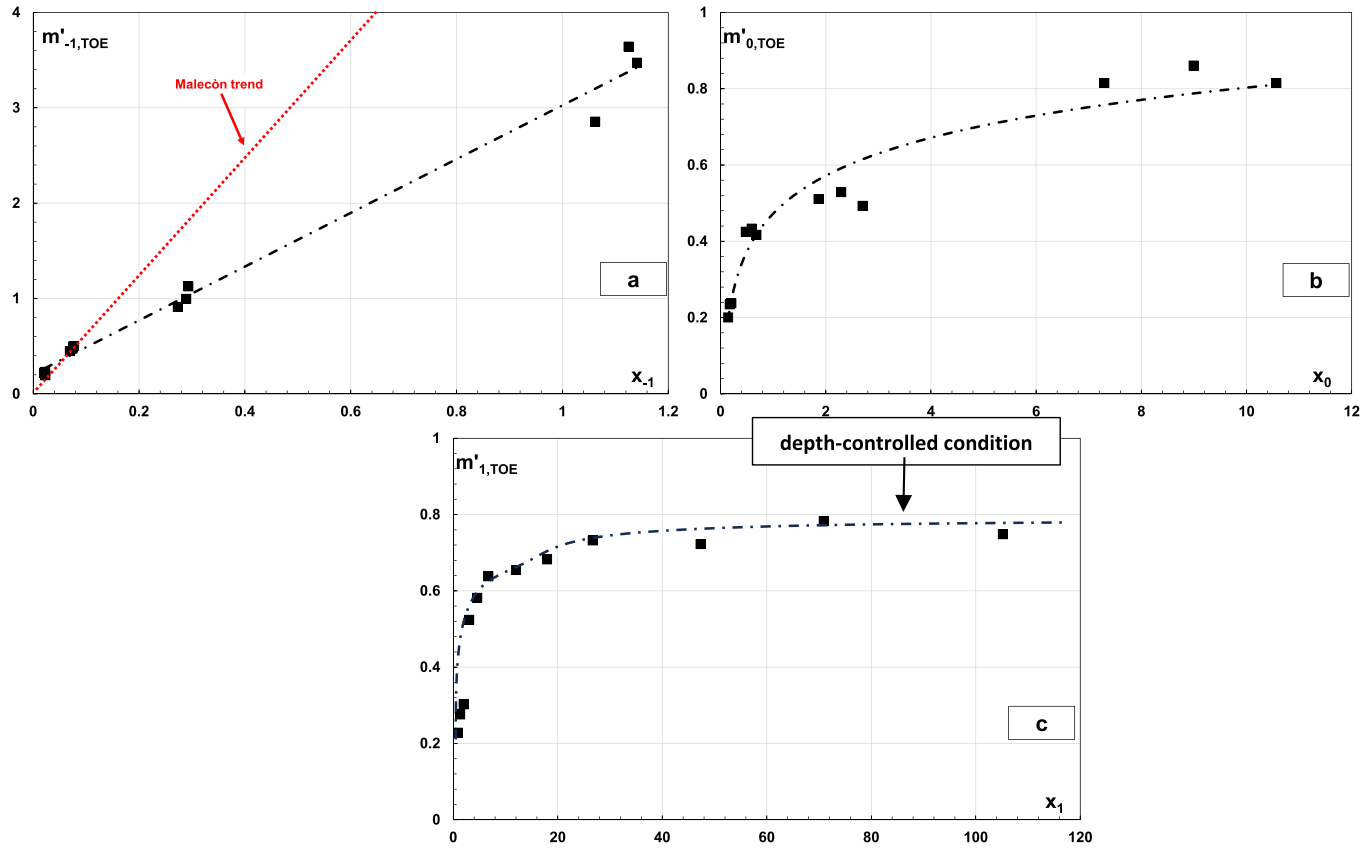

Fig. 11. Non dimensional spectral moments in the function of x_n (van Gent (1999) slope 1/100). E_{rms-N} is calculated assuming a Gaussian narrow band process.

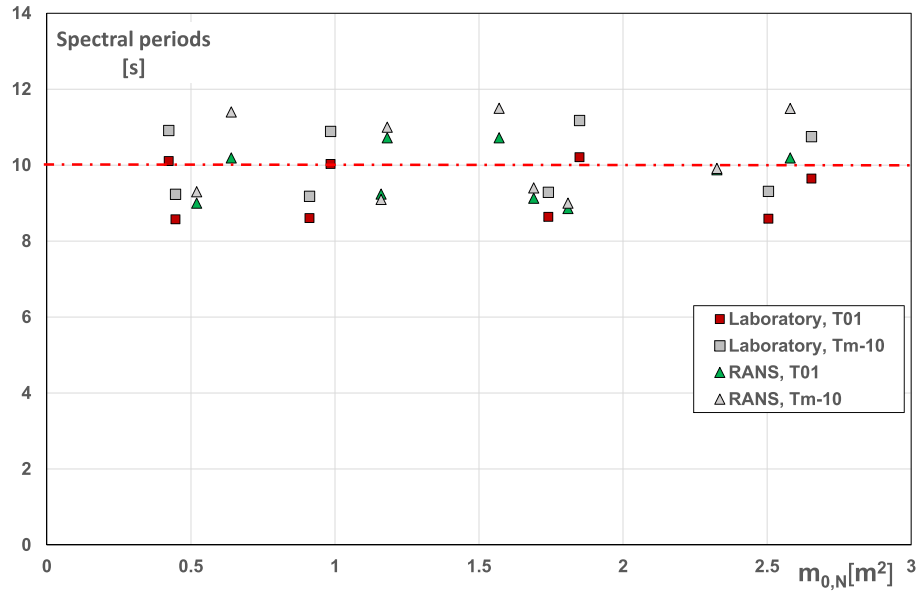

Fig. 12. Mean spectral periods as a function of wave energy (Nearshore data).

therefore, create the conditions for the rise of spurious (false) correlations, which are independent of the physics of the processes. We will return to this point in Section 3.3.

It is finally worth highlighting that the sign of the trends in Figs. 13 and 14 (whether increasing or decreasing) is of little importance for this discussion, as it depends on how the experiments were designed. While Malecòn's experiments used a single value of h_{TOE} and varied the wave parameters in the Nearshore zone, van Gent conducted his tests with almost the same offshore wave height, changing the local water depth instead. This causes the experimental points to be mirrored.

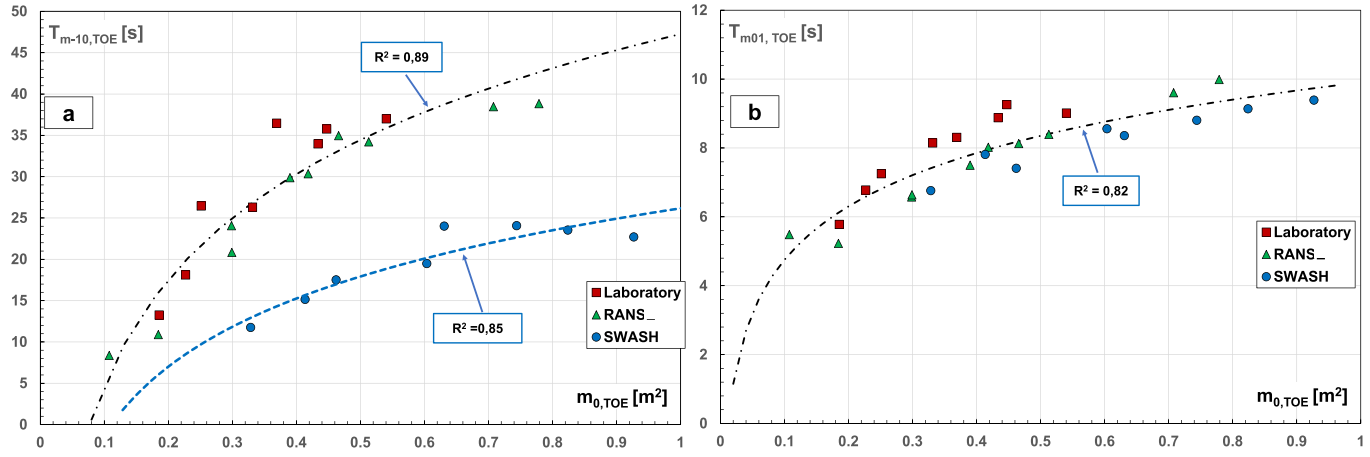

Fig. 13. Relationships between wave energy and mean spectral periods for the Malecòn experiments. Panel a: $T_{-10,TOE}$; panel b: $T_{01,TOE}$.

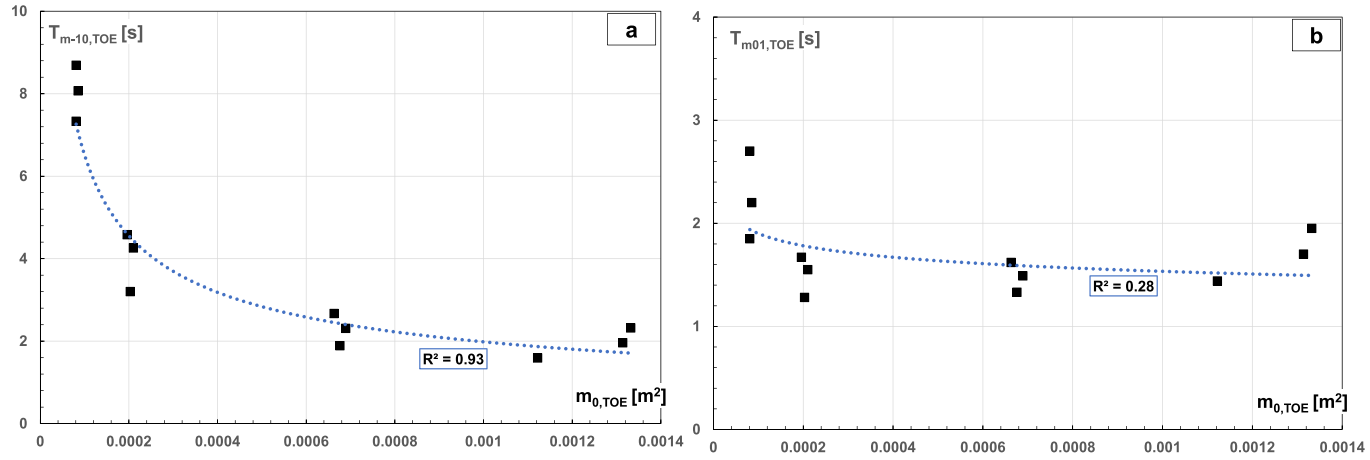

Fig. 14. Relationships between wave energy and mean spectral periods for van Gent's experiments.

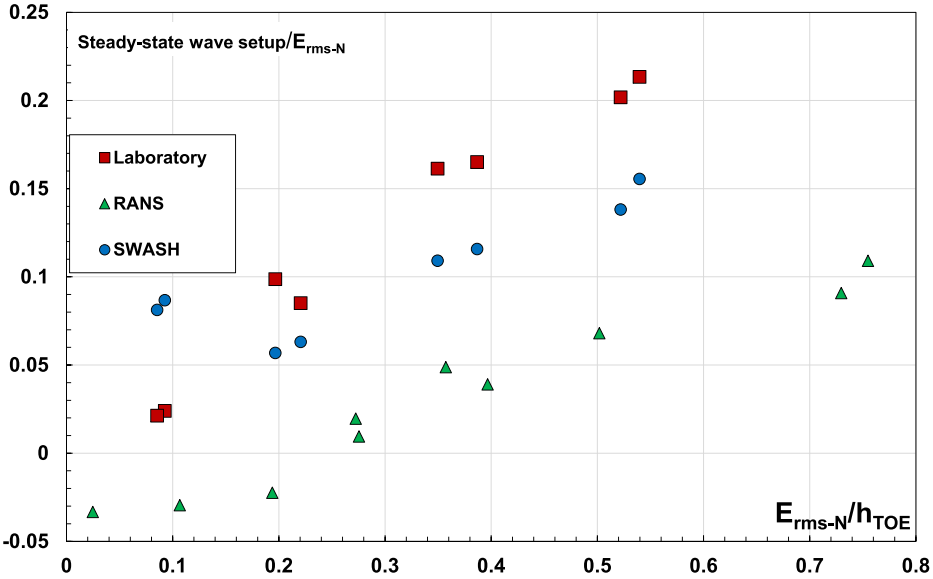

Fig. 15. Laboratory and numerical wave setups at the toe of the wall.

3.2. Analysis of the mean (steady-state) wave setup

The mean, steady-state wave setup (shortly referred to as "wave setup" hereinafter) is the average of the surface elevation signal at the location of the wall. The uneven profile of the Malecòn foreshore led to values of this parameter particularly high, which both the numerical models were observed to underestimate (Fig. 15).

The underestimation is particularly large in the RANS experiments, most likely because of the mass-source generation condition, which allows the water to leave the domain on the upwave side.

Although this bias has a limited effect on the spectral moments, its impact on wave overtopping is predictably more stringent, **as discussed in more detail in** Section 3.3.

3.3. Analysis of the mean overtopping rate

The starting point of our analysis is to compare laboratory and numerical data with EurOtop's prediction formulae for plain walls.

The formulae read:

$$q^* = \begin{cases} 0.05\ exp\left(-2.78 \bullet \dfrac{R_c}{H_{m0,TOE}}\right) & for\ h^* > 0.23 \\ \sqrt{\left(\dfrac{gT_{m-10}^2}{2\pi\, h_{TOE}}\right)} \bullet min\left[0.011\ exp\left(-2.2 \bullet \dfrac{R_c}{H_{m0,TOE}}\right); 0.0014\left(\dfrac{R_c}{H_{m0,TOE}}\right)^{-3}\right] & for\ h^* \le 0.23 \end{cases} \quad (18)$$

in which $q^* = \frac{q}{\sqrt{g \bullet H_{m0,TOE}^3}}$ is the non-dimensional flow rate, and the parameter h^* (see section 2.1.1) discriminates the occurrence of pulsating ($h^* > 0.23$) or impulsive loadings ($h^* \le 0.23$).

Like all the empirical formulae, the relationship between overtopping rate and wave height in Eq. (18) is markedly nonlinear, halfway between the exponential and the power forms.

However, the most peculiar aspect from a conceptual point of view concerns the effect of wave period; counterintuitively, the role of T is negligible for large water depths ($h^* > 0.23$), just where the PSD is narrow-banded, and the waves exhibit a clear characteristic frequency. On the other hand, T affects q under shallow water conditions ($h^* \le 0.23$), when the complex shape of the wave spectrum makes it arduous to individuate a characteristic frequency. In particular, the choice of $T_{m-1,0}$, strongly related to the "surf-beats" components, is not plainly justified, due to the lack of reliable shallow water data we discussed in Fig. 4.

The comparison in Fig. 16 shows that the EurOtop curve (solid line) underpredicts the laboratory data while overestimating the numerical results. However, most points lie within or close to the 90% confidence bands (broken curves), indicating that the observed scatter is consistent with the inherent variability of the overtopping process. From this perspective, both the numerical approaches predict the overtopping rate reasonably well.

Even so, we aim to gain a deeper insight into why the numerical results lay systematically beneath the physical model.

In the sections below, this is accomplished by assessing, one by one, the relationships between numerical and laboratory overtopping rates, q, and the predictors of Eq. (18), i.e., crest freeboard, wave energy at the toe of the wall, and mean spectral periods. The approach adopted is a variant of the Added Variable Plot method (Draper and Smith, 1998), which the authors successfully applied in analyzing wave transmission (Buccino et al., 2013) and wave reflection (Buccino et al., 2018).

Essentially, we exploit a sequence of simple linear regression models; let X_1 be a predictor and let the equation:

$$q = a + b \bullet X_1 + \varepsilon_1 \quad (19)$$

represents a regression model, which links it to the overtopping rate.

The effect of a second predictor, say X_2, is assessed by regressing this new quantity on the residuals, ε_1; since X_1 and ε_1 are inherently

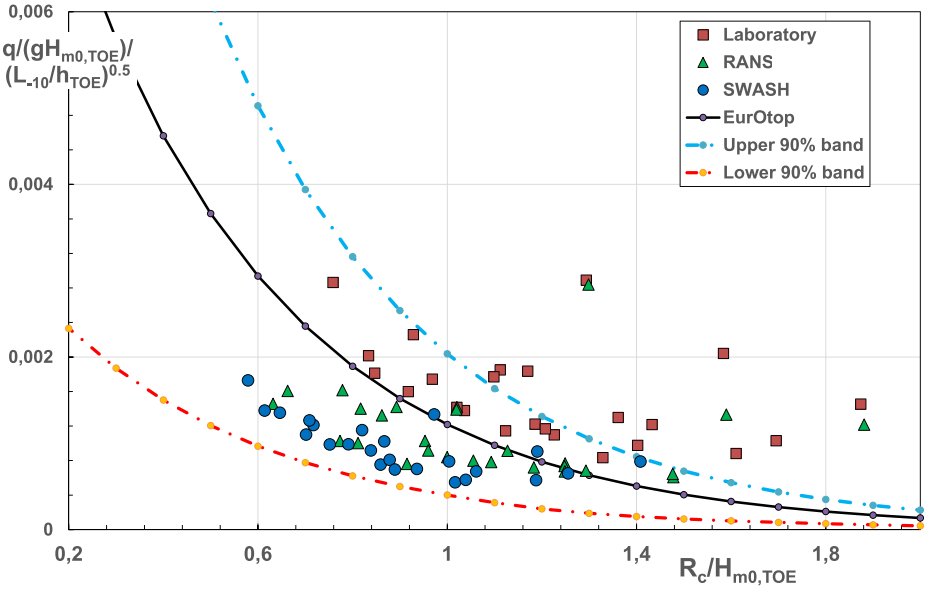

Fig. 16. Laboratory and numerical data on the EurOtop formula non-dimensional plane. Note that all the data are within the impulsive domain $h^* \le 0.23$.

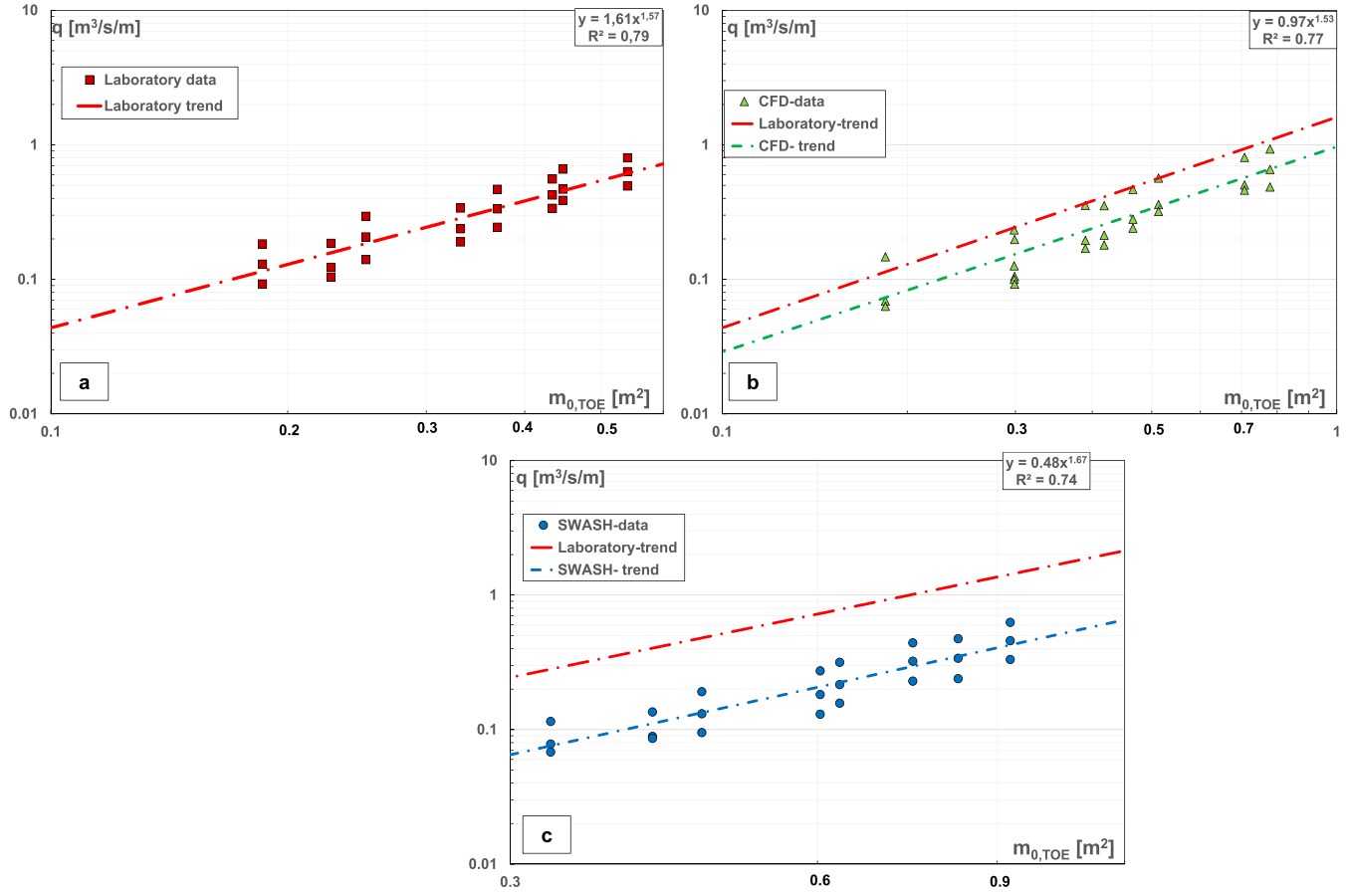

Fig. 17. Laboratory and numerical flow rates vs. wave energy at the toe of the wall.

independent, this allows us to reduce the non-causal effects due to the correlation between X_2 and X_1 (spurious correlation effects).

Besides providing detailed information on the behavior of the numerical models, the procedure described above helps us to shed some light on the role of the different variables involved in the overtopping process. This is with particular emphasis on mean spectral periods, which are affected by the correlation structures shown in Figs. 13 and 14.

3.3.1. *The role of wave energy and crest freeboard*

In panels a to c in Fig. 17, the laboratory and numerical values of q are plotted against the wave energy at the toe of the wall, $m_{0,TOE}$. Since the relationship between these variables is significantly nonlinear, as discussed earlier, the data are fitted with a power function, which is linearized into:

$$ln(q) = b \bullet ln\left(m_{0,TOE}\right) + ln(a) + \varepsilon_z \tag{20}$$

Then, to assess the influence of the crest freeboard independently of the wave height, Fig. 18 charts R_c vs. the residuals ε_z.

The inspection of the graphs suggests that both the numerical models account for the effect of the crest freeboard properly (Fig. 18); however, RANS slightly overpredicts the lower freeboards, as indicated by the green line in panel b. On the other hand, for a given value of $m_{0,\,TOE}$, the two software give a smaller q than laboratory tests (Fig. 17), which explains the underestimations found in Fig. 16. The bias is particularly large for SWASH.

Reasonably, however, the observed behavior is due to the wave setup underprediction shown in Fig. 15. To take this effect into account, Fig. 19 replots the flow rates against the quantity:

$$\zeta_{1/4} = \left(\text{wave setup} + 1.27\sqrt{m_{0,TOE}}\right) \tag{21}$$

which represents the average of the highest one-fourth water levels in a Gaussian wave process.

RANS and laboratory data follow now approximately the same trend, while SWASH lies only moderately below.

From a physical point of view, this result expresses the simple concept that the amount of wave overtopping cannot depend solely on the variance of the wave fluctuations, but rather on the upper tail of the distribution. Indeed, this is the rationale that has prompted several authors in the literature (van der Meer, 1995; Hedges and Reis, 1998; Mase et al., 2013) to relate overtopping rate and run-up heights with low exceedance probability, (e.g., $R_{u2\%}$).

However, it should be noticed that $\zeta_{1/4}$ is calculated in the absence of the wall and is therefore not a runup statistic.

3.3.2. *Influence of the spectral periods*

$T_{m\text{-}10}$ and T_{01} are parameters that account for the effect of the wave energy distribution in the frequency domain in the long and short-wave range, respectively. The most straightforward and intuitive way to assess their role is by comparing Figs. 20–22.

Fig. 20 plots the mean spectral periods against the flow rate q and shows significant increasing trends, consistent with the findings of several authors in the literature (van Gent, 1999; Altomare et al., 2016). Moreover, the values of the R^2 statistics are quite high, unlike the "Nearshore" peak period $T_{p,N}$ in Fig. 21, whose degrees of correlation are very weak or negligible. Hence, the spectral periods seem to have a larger explanatory power.

However, once q is made independent of m_0, and the wave periods are plotted against ε_z, the correlation disappears wherever (Fig. 22).

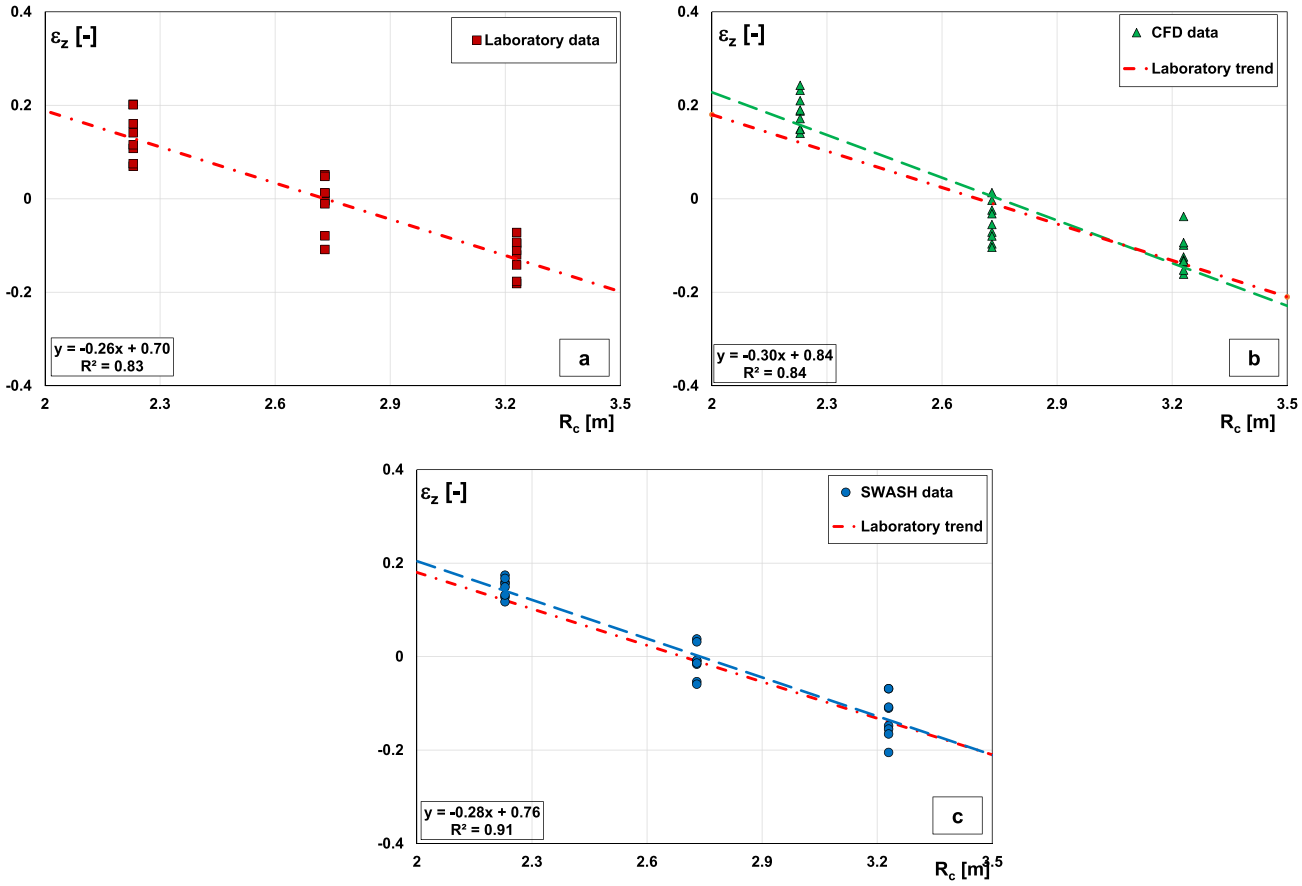

Fig. 18. Reduction of wave overtopping in response to crest freeboard.

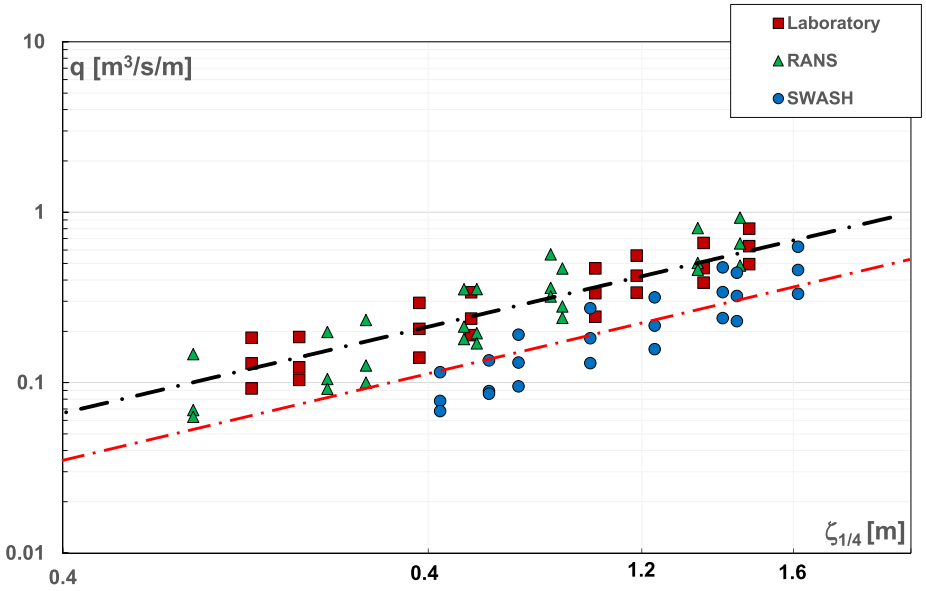

Fig. 19. Laboratory and numerical flow rates as a function of $\zeta_{1/4}$.

This result indicates that $T_{m\text{-}10}$ and T_{01} do not contribute to the prediction of q more than $T_{p,N}$, and the correlation observed in Fig. 20 essentially results from the relationship with the wave energy we observed in Fig. 13. It is, therefore, a spurious correlation effect rather than a real physical relationship.

In Appendix A.2, we check this interesting outcome against the runup data of van Gent (1999), one of the first studies to highlight the role of $T_{m\text{-}10}$ in the wave-structure interaction processes. The analysis

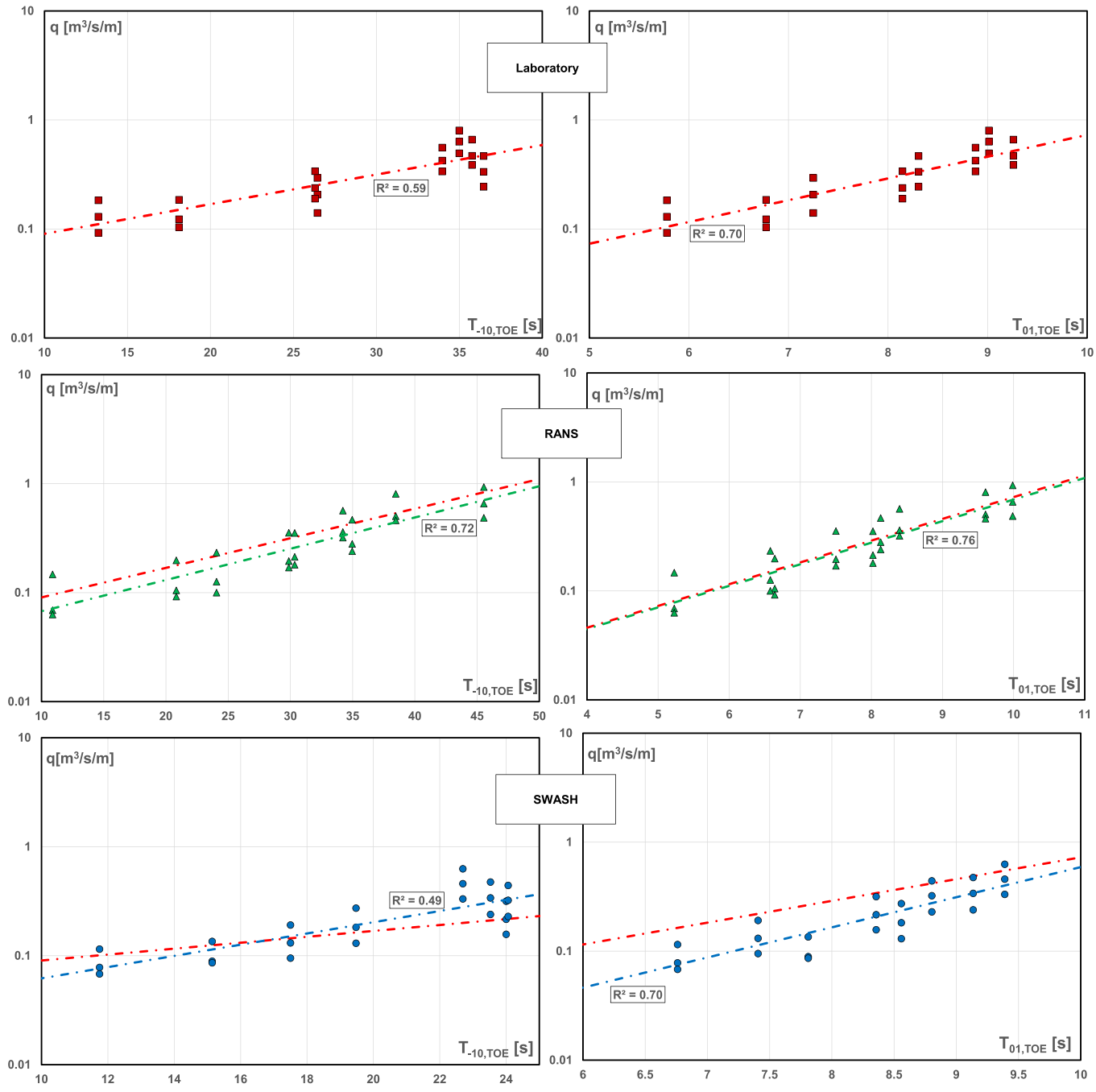

Fig. 20. Laboratory and numerical flow rates as a function of the mean spectral periods.

outcomes are remarkably consistent with those discussed above.

3.3.3. *Predicting the overtopping rate in the surf zone*

According to the foregoing analysis, the overtopping of a vertical seawall in the surf-zone can be predicted just in the function of the crest freeboard, and some water level statistics related to the upper tail of the distribution of the surface elevations at the toe of the structure, say $= q(R_c, \zeta_f)$.

This is confirmed in Fig. 23, which plots the values of q for the entire PWS dataset (48 data, two water levels) against the ratio $R_c/\zeta_{1/4}$; the graph also includes the results from the numerical models.

The data are definitely little scattered, and each series follows a very predictable trend, resulting in high values of the R^2 statistics. RANS experiments can be assimilated to the same regression equation as the laboratory data (solid curve, $R^2 = 0.92$), which indicates a satisfactory simulation of the overtopping process. On the other hand, SWASH tends to yield to some systematic underpredictions, as previously noticed by Suzuki et al. (2017). Fig. 23 also stresses out the role of the wave setup, which is treated with some ambiguity in the literature, so that it is not included explicitly among the overtopping predictors. This might be either because the EurOtop database includes only few data in the surf-zone (Fig. 4), or simply because no information on this quantity was available for the analysis.

However, the influence of wave setup clearly emerges from Fig. 24, where it can be seen that the plot of q in the function of the sole wave variance $m_{0,TOE}$ leads the spreading of data to increase significantly.

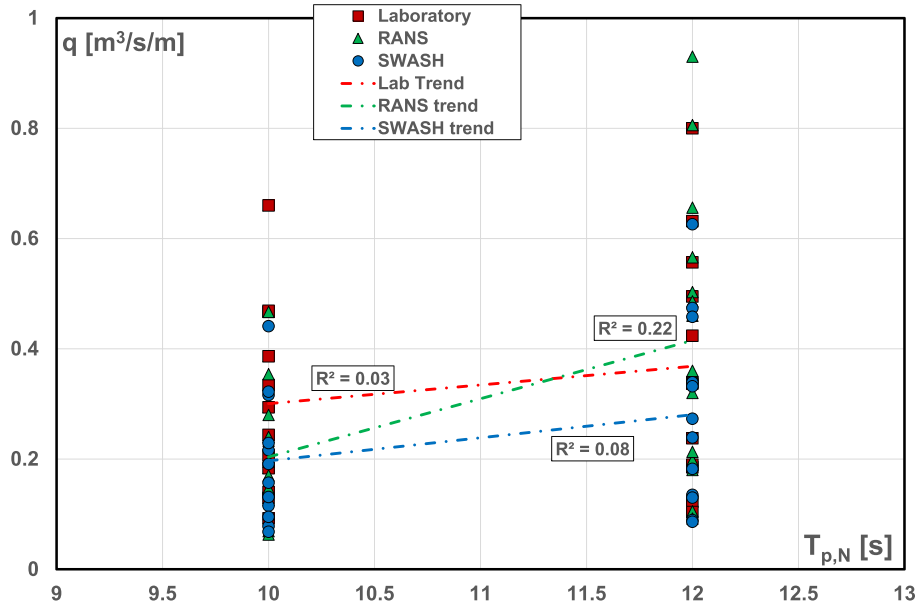

Fig. 21. Laboratory and numerical flow rates as a function of the mean "Nearshore peak period".

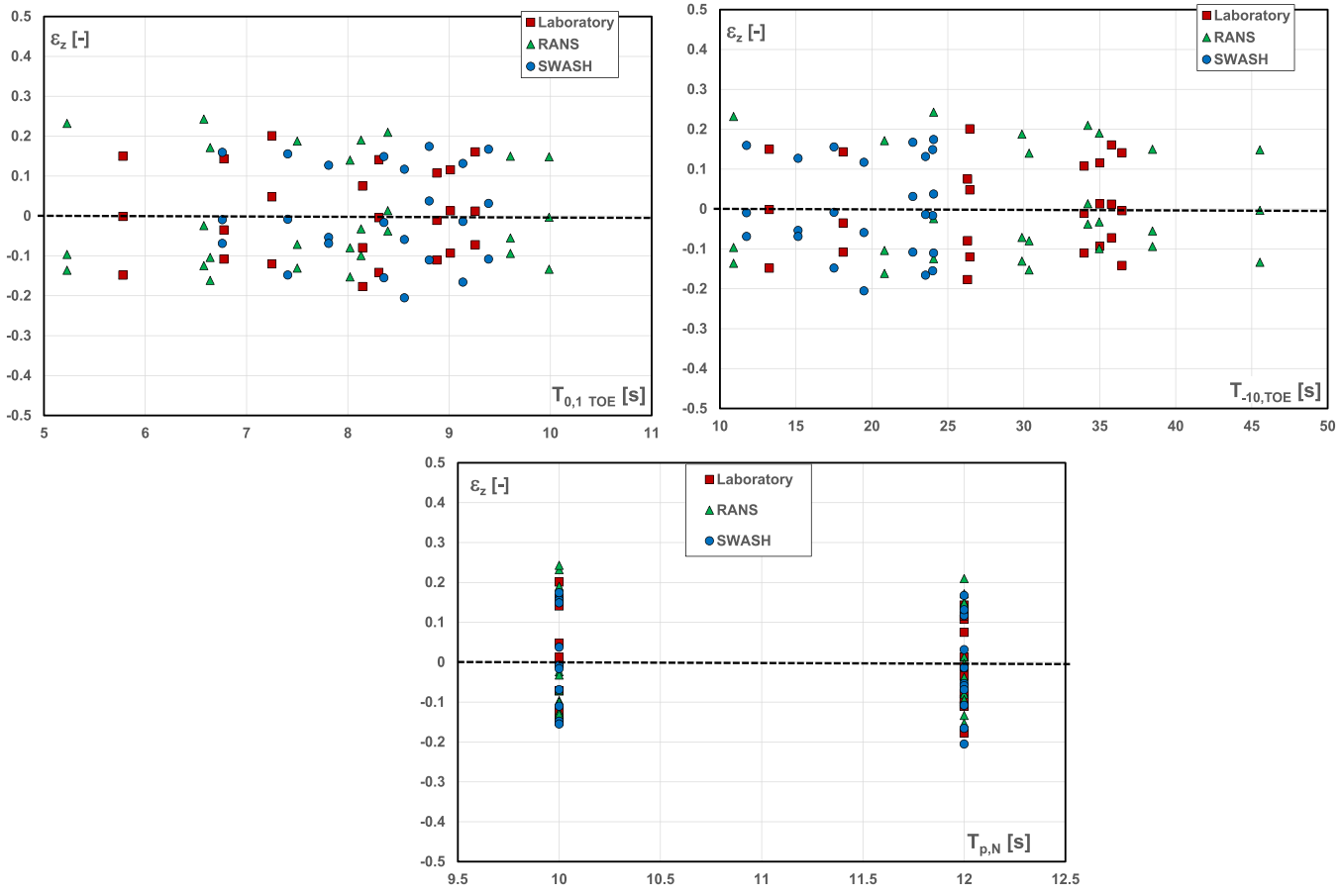

Fig. 22. Relationships between the wave periods and the residuals ε_z.

4. Discussion

Our findings indicate that RANS and SWASH capture the general physics of the processes investigated satisfactorily. Remarkably, this is true for a wide range of phenomena, including the spectral moments' trend with varying "Nearshore" wave conditions (Fig. 9), the correlation relating wave energy and mean spectral periods (Fig. 13), and the relationships between the overtopping rate and the wave properties at the

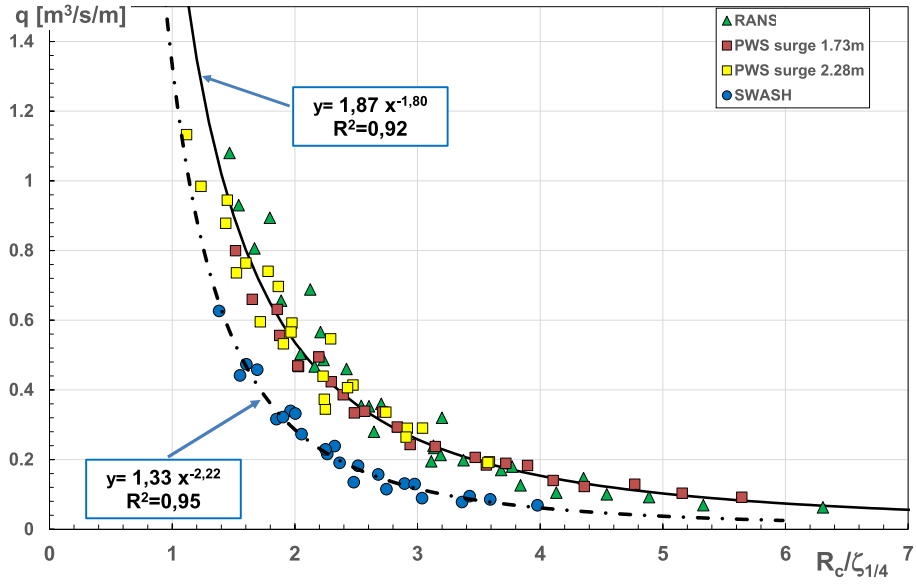

Fig. 23. Laboratory and numerical values of q *vs* $R_c/\zeta_{1/4}$.

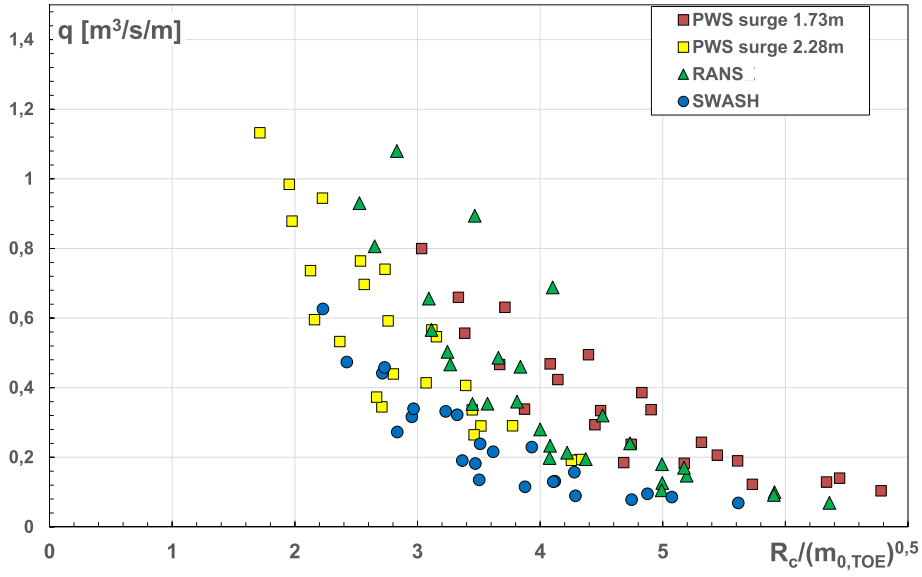

Fig. 24. Laboratory and numerical values of q *vs* $R_c/(m_{0,TOE})^{0.5}$.

toe of the wall, either in the frequency or in the time domain (Figs. 17, 19, 20 and 23). Therefore, the difference between the performance of the numerical approaches is merely quantitative. RANS experiments are, in fact, in good agreement with the physical model, which also leads to excluding the presence of major scale effects in the laboratory experiments.

On the other hand, SWASH suffers from two main biases: it over-predicts the high-frequency components of the surf zone spectra and systematically underpredicts the overtopping rate. Neither of these, however, are new in the literature.

PSDs very similar to those shown in Fig. 10 can be found, e.g., in Fig. 18 of Zijlema et al. (2011), which refers to the laboratory experiments of Boers (1996). Although Zijlema et al. do not provide specific comments on this point, one notices that SWASH adequately predicts the surf-beats, while the high-frequency components are overestimated. However, the ratio between numerical and laboratory spectral moments reaches at most 1.5, whereas for our data we calculated 1.9; this is likely an effect of the beach angle, which in Boers (1996) was as mild as 1:40. In any case, the tendency at overpredicting the shortwave peaks seems an inherent drawback of SWASH (see also Fig. 16 of Zijlema et al., 2011).

As for the underprediction of the overtopping rate, Suzuki et al. (2017) analyzed 124 experiments of shallow water sloping dikes and found an average underestimation factor of about 0.80; for the Malecòn we have 0.69, which is essentially in line. The tendency at under-predicting the laboratory measurements is likely related to the simplifications introduced by SWASH in the vertical resolution of flow, which are expected to be especially relevant in the case of vertical structures. However, given the high variability of the overtopping process, these values can be considered reasonably accurate; engineers can readily

account for the bias in practical applications by multiplying the numerical overtopping rate by 2.

From a physical point of view, an essential result of this study concerns the correlation between the spectral moments in the surf zone. The joint analysis of laboratory and numerical data has shown that a relationship is created between wave energy (m_0) and spectral periods (T_{m-10}, T_{01}) despite these quantities being independent outside the surf zone (Figs. 12 and 13). The relationships apply unless a "depth-controlled" condition is attained because of breaking.

According to the saturated breakers theory by Le-Mehautè (1962), we did not observe this condition on the Malecon's steep foreshore but on the mild beach in Fig. 11; in this graph, the first-order moment of the PSD becomes saturated, which weakens the relationship between m_0 and T_{01} in Fig. 14. Conversely, since surf-beats are almost unaffected by wave breaking, the link with T_{m-10} is hardly destroyed.

Therefore, we expect wave energy to correlate with both spectral periods in steep surf zones while only with T_{m-10} on mild beaches.

These correlation structures are relevant because they create spurious relationships with the variables related to the wave-structure interaction processes. The Added Variable Plot analysis of the Malecòn overtopping rates in Section 3.3 and the runup data of van Gent (1999) in Appendix 2 leads to consistent conclusions: the influence of T_{m-10} and T_{01} is spurious, and depends on their relationship with m_0. If we remove the effect of this correlation from the data, the mean spectral periods do not explain the output variables more than the peak period of the waves outside the surf zone. In other words, the processes are negligibly affected by the shape of the PSD.

The overtopping discharge is instead strongly related to the high percentiles of the distribution of the surface elevation at toe of the wall; consistently, in Fig. 23 laboratory and numerical data are very well predicted in terms of the variable $\zeta_{1/4}$, which represents the average of the highest one-fourth water levels in a Gaussian wave process. The relationships reported in the graph, which are at the prototype scale, exhibit a very high R^2 index, indicating a remarkable prediction power.

From a physical perspective, this finding is not actually new, because it corroborates, in effects, the approach of many authors who have developed relationships to relate overtopping rate and extreme runup heights (Hedges and Reis, 1998; Mase et al., 2013). However, compared to those extreme runup statistics, $\zeta_{1/4}$, is much simpler to calculate.

The results of Section 3.3.3 finally stress out the role of the wave setup in the overtopping process. Despite being a leading variable in surf zone problems, it is treated with some ambiguity in the literature, while it deserves more attention. Sometimes researchers consider it as a "self-accounted" quantity, as it is correlated very strongly with the height of the breakers (EurOtop, 2018). However, the correlation law is not unique, but depends on the topography of the seabed as well as, like for RANS in Fig. 15, on possible model effects in laboratory or numerical experiments.

For this reason, it should be included explicitly in the prediction formulae.

5. Conclusions

This article has addressed spectral evolution and wave overtopping in an uneven surf zone. We compared laboratory and numerical results with a degree of depth certainly greater than previous literature; moreover, the adopted methodologies allowed focusing on aspects of the physics of the processes, which are relevant in engineering applications. Nevertheless, the main limitation is the narrow dataset, which prevented the development of adequately robust prediction formulae. Therefore, the most urgent prerequisite for future research developments is the availability of reliable data, in which information on wave overtopping at structures located well inside the surf zone is joined with details about the wave properties, both in the time and frequency domain. As we showed at the beginning of this work, the lack of such data is a weakness of the literature; the methodologies discussed in this paper can be readily applied to the new data, in order to confirm or confute our conclusions.

However, the capability of phase-resolving numerical models to capture the physics of the processes suggests that the new data should not necessarily come from laboratory experiments. Numerical models allow, in effect, to vary all the relevant parameters without the unavoidable limitations of the physical models (e.g., scale limitations, shape of the foreshores, wavemaker characteristics, etc.). In a new paper currently under review, we carry out a detailed parametric study using SWASH and provide new arguments on the effect of spectral periods on wave overtopping. Moreover, we develop a new formula for predicting the overtopping rate, which is uniformly valid from deep to extremely shallow water. Net of the inherent bias of SWASH, we extensively discussed in this research, the new formula resulted surprisingly consistent with a wide array of laboratory data.

CRediT authorship contribution statement

Mariano Buccino: Conceptualization, Methodology, Validation, Writing – review & editing. **Angela Di Leo:** Software, Investigation, Visualization. **Sara Tuozzo:** Software, Investigation, Visualization. **Luìs F. Còrdova Lopez:** Investigation, Formal analysis. **Mario Calabrese:** Supervision, Writing – review & editing. **Fabio Dentale:** Methodology, Software, Formal analysis.

Declaration of competing interest

The authors declare that they have no known competing financial interests or personal relationships that could have appeared to influence the work reported in this paper.

Data availability

Data will be made available on request.

Acknowledgements

This paper has exploited results of physical model tests carried out at the University of Napoli Federico II in the frame of a project for the rehabilitation of the Malecòn Traditional seawall. The contract of the project was stipulated between Instituto Politécnico José Antonio Echeverría of l'Habana (Cuba) and C.U.G.RI. (Consorzio inter-Universitario per la previsione e la prevenzione dei Grandi Rischi). The authors wish to gratefully acknowledge Professors Paolo Villani and Eugenio Pugliese Carratelli for their competence in the analysis of the processes and in numerical simulations. Dr Daniela Salerno, Dr Andrea Bove and Alessandro Capobianco are also acknowledged for their assistance in testing.

APPENDIX A.1

A.1.1. Grid Sensitivity study for CFD-RANS

To investigate the effect of grid size on the results of *CFD-RANS*, a cnoidal wave train with $H_{1/3,N} = 7.5m$ and $T_{1/3,N} = 10s$ was propagated first over the shoal and then with the wall in place (wall height +3.96 m). The test was replicated with eight rectangular grids, whose characteristics are

summarized in Table A.1.I.

The horizontal spacing, Δx, was chosen so that the number of points in a shallow water wavelength (L_{TOE}) would be gradually increased. On the other hand, Δz is selected to maintain the aspect ratio around 2.5, apart from C278 and M278 that have the same Δx. The number of points in a nominal breaker height ($H_b = 0.55\ h_{TOE}$) reported in the last column of the table, is an indicator of the vertical resolution of the grid.

Table A.1.I
Grids characteristics.

GRID CODE	Δx[m]	#">#points/L_{TOE}	Δz[m]	#">#points/H_b
A20	2.9	20	1.2	2
A30	1.9	30	0.8	2
A40	1.5	40	0.6	3
A60	1.0	60	0.4	5
A80	0.7	80	0.3	6
A160	0.4	160	0.15	13
C278	0.25	278	0.30	6
M278	0.25	278	0.15	13

Figure A.1.1 shows the wave envelope along the flume in the absence of structure, whereas the curves of the overtopping volume are given in Figure A.1.3.

Figure A.1.2 plots, instead, the time-averaged kinetic turbulent energy for a fluid layer at the still water and two different grid sizes, namely A160 and A80. The kinetic energy rises abruptly in the neighbours of the breaker line and remains significantly high through the narrow surf-zone. Therefore, the unphysical increase of turbulence prior to the onset of breaking discussed in Larsen and Fuhram (2018) and Li et al. (2022) is not observed, mainly because of the large-scale modelling, along with the limited extent of the shoal compared to the wavelength.

More in general, wave propagation appears scarcely affected by the grid size from A80 onwards, while the overtopping process tends to converge (on average) already from A40. The mean overtopping rate among the grids from A40 to M278 ranges by a maximum of 5%.

Based on previous outcomes, we used grid A80 from the wave generation up to 100 m from the wall. Shorewards, grid A160 was chosen, to keep the maximum vertical resolution in the innermost part of the surf zone as well as at the wall.

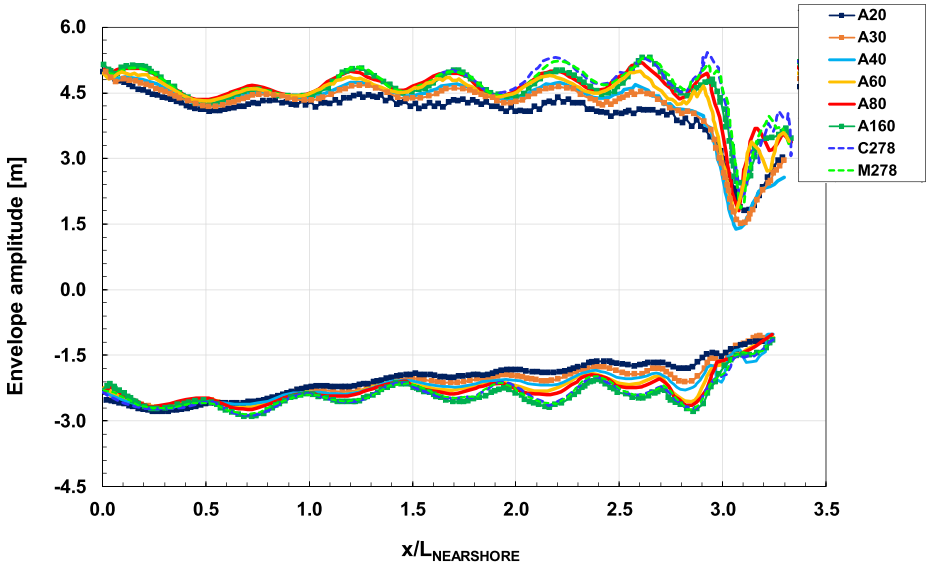

Figure A.1.1. Wave envelope along the numerical flume (no wall).

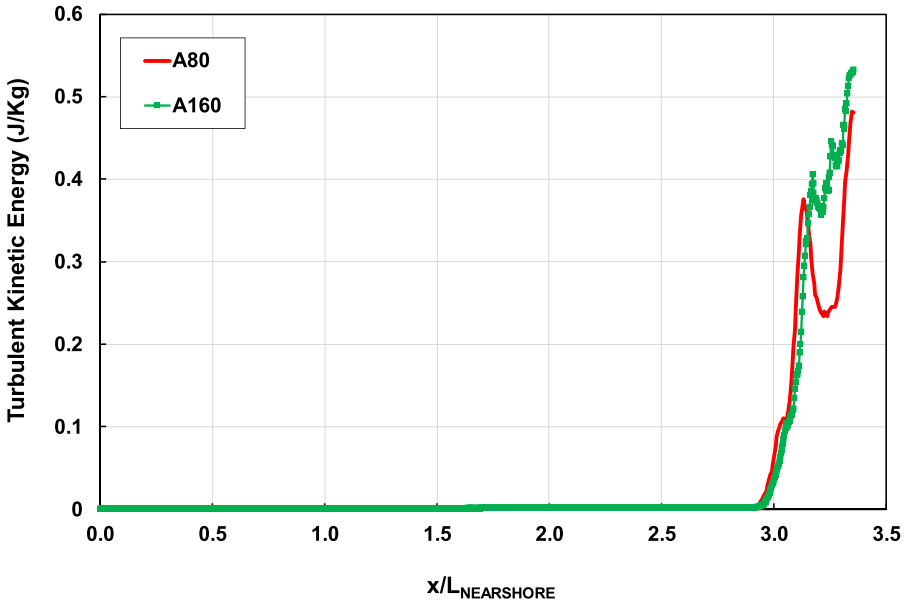

Figure A.1.2. Time-averaged Turbulent Kinetic Energy at the still water level (no wall).

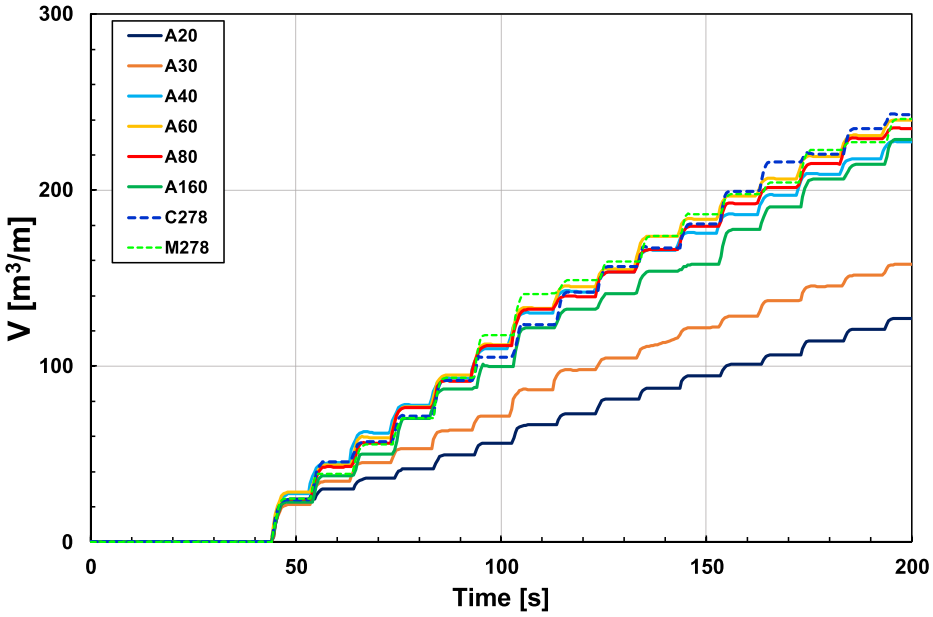

Figure A.1.3. Curves of overtopping volume.

Appendix A.1.2. On the effect of SWASH's parameters

Grid Spacing

A PWS random wave experiment ($H_{m0,N} = 5.4$ m and $T_{p,N} = 10$s) was run for six different grid spacings, keeping the Manning coefficient $\nu = 0$. The grid spacings ranged from $\Delta x = 0.5$ m to $\Delta x = 3.0$ m, corresponding to a number of points per shallow-water wavelength varying from 20 to 128.

The left panel in Figure A.1.4 shows the Power Spectral Density (PSD) at the location of the wall, whereas the right panel reports the mean overtopping rates, q.

Consistently with Suzuki (2014), convergency is observed solely on PSD, whereas the overtopping discharge exhibits remarkable scatter. When Δx is reduced from 3.0 m to 1.0 m q more than doubles, while the trend reverses for the finer grids. Thus, wave overtopping becomes saturated at $\Delta x =$ 1.0 m, which was selected as the final grid for testing (Suzuki, 2014).

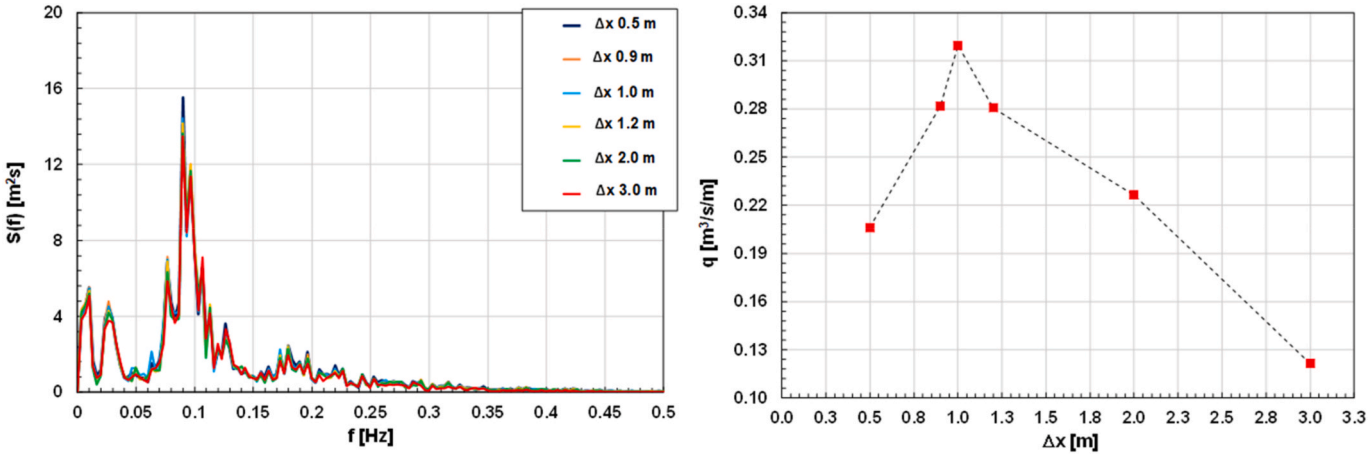

Figure A.1.4. Effect of grid spacing on Power Spectral Density (left panel, no wall) and wave overtopping (right panel, Malecon's current height). $H_{m0,N} = 5.4$m $T_{p,N} = 10$s. Manning coefficient is 0.

Manning coefficient

The role of the Manning coefficient was investigated for the same wave attack, keeping $\Delta x = 1.0$ m.

The left-hand panel in Figure A.1.5 indicates that the impact on wave spectrum is weak overall, and mainly affects the low-frequency components. Increasing ν results in a surf-beats dampening, which leads to a reduction of both m_{-1} (up to −15%) and m_0 (−5%), while the first order spectral moment increases (up to +11%).

On the other hand, the effect on wave overtopping is significant, as highlighted in Suzuki et al. (2011). The right panel in Figure A.1.5 shows that the mean overtopping discharge q decreases linearly with the Manning coefficient. As ν transitions from 0 to 0.1 $m^{-1/3}$ s, the mean overtopping rate decreases by 1/3.

The best agreement with the results of the physical model is thus obtained with $\nu = 0$ $m^{-1/3}$s.

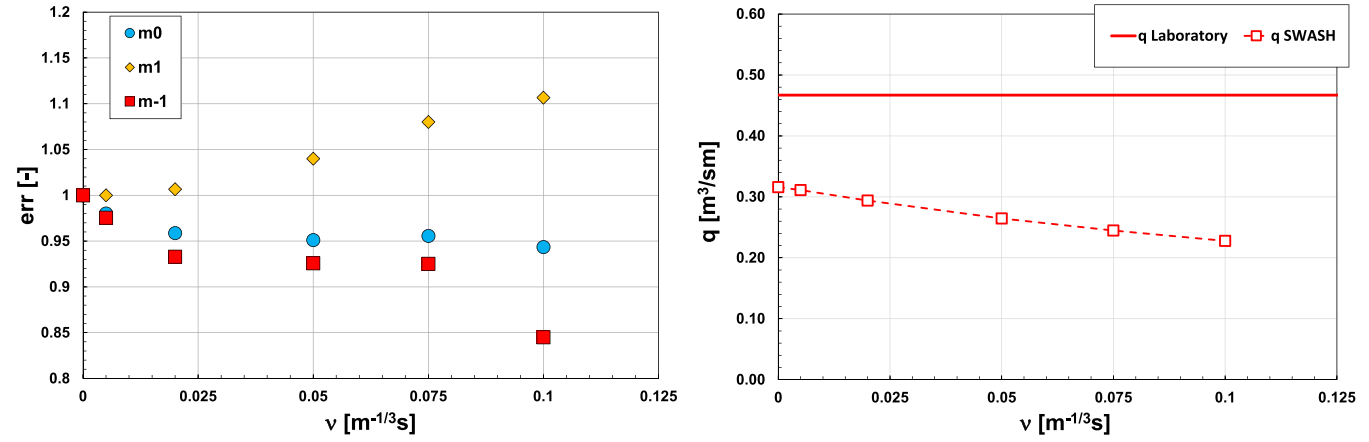

Figure A.1.5. Effect of Manning coefficient on Power Spectral Density (left panel, no wall) and wave overtopping (right panel, Malecon's current height). $H_{m0,N} = 5.4$m $T_{p,N} = 10$s. *Grid spacing is 1.0m.*

Appendix A.2

This Appendix exploits the runup data of van Gent (1999) to test the conclusions of Section 3.3.2 concerning the role of the mean spectral periods. The research of van Gent (1999) was, in effect, one of the first studies to highlight the role of low-frequency spectral components in the interaction between waves and shallow water structures.

The author measured the 2% exceedance runup height, $z_{2\%}$, on impermeable sloping dikes inclined at 1:4 and 1:2.5. The structures rested in shallow water on two planar beaches with angles 1/100 (discussed in Section 3.1.2) and 1/250. The offshore spectra had an approximately constant energy ($H_{m0,deep} \cong 0.14$ m) and a single peak with three modal frequencies. The water depth at the location of the structures was systematically varied to change the shape of the incoming PSD.

The analysis steps, which follow the principles discussed in Section 3.3, can be summarized as follows.

It was found that the relationship between wave runup and local wave height, $H_{m0,TOE}$, can be described by the log-model:

$$ln\,(z_{2\%}) = 0.57 + 0.77 \bullet ln\left(H_{m0,TOE}\right) + \epsilon_H \tag{A.2.I}$$

whereas the residuals ϵ_H can be related to the structures' slope, $tan\ \alpha$, according to the formula:

$$\epsilon_H = 0.33 + 0.33 \bullet ln(tan\ \alpha) + \epsilon_\alpha \tag{A.2.II}$$

Thus, summing (A.2.I) and (A.2.II) leads to the following predictive equation:

$$ln\ (z_{2\%}) = 0.88 + 0.77 \bullet ln\left(H_{m0,TOE}\right) + 0.33 \bullet ln(tan\ \alpha) + \epsilon_\alpha = Z + \epsilon_\alpha \quad \text{(A.2.III)}$$

which explains about 95% of the data variance, as shown in panel a of Figure A.2.1.

Then, in the panel b of the same graph, the residuals ϵ_α are regressed against the offshore peak period, $T_{p,off}$; the model:

$$\epsilon_\alpha = -0.33 + 0.47 \bullet T_{p,off} + \epsilon_{Tp} \quad \text{(A.2.IV)}$$

is statistically significant and explains nearly 62% of the (residual) scatter.

It is now evident from panels c and d that there are no relationships between ϵ_{Tp} and the mean spectral periods T_{m-10} and T_{01}. These graphs are perfectly consistent with Fig. 22 and corroborate the conclusion that the distribution of wave energy in the frequency domain, either in the low or high range, does not actually affect the wave-structure interaction process. Noteworthily, though, this does not imply an independence of the wave period "tout court", as we showed the data are, in effect, correlated with the offshore peak period.

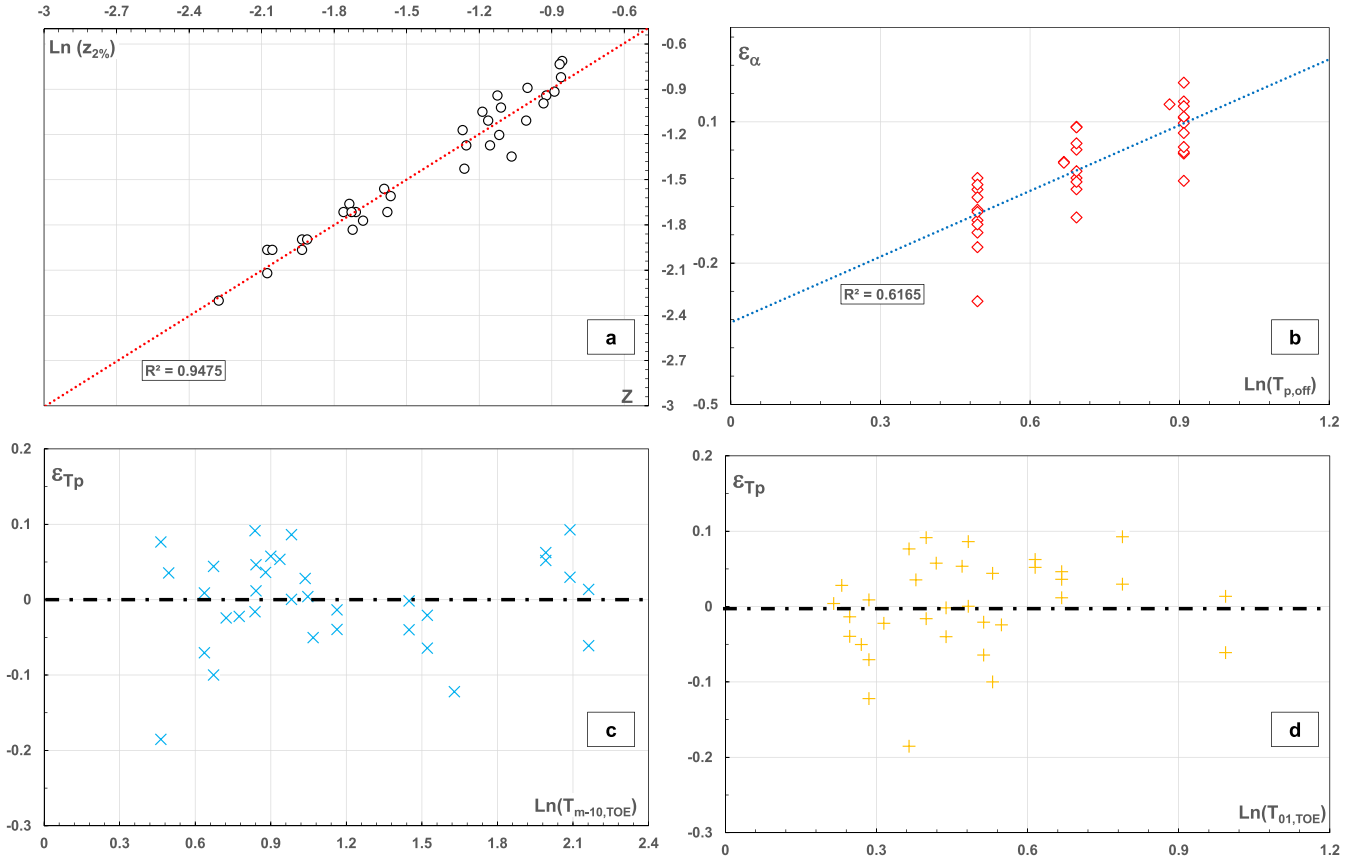

Figure A.2.1. Regression plot analysis of van Gent's runup data.

Van Gent's conclusions regarding the influence of T_{m-10} result then from a spurious correlation that arises as wave runup is nondimensionalized by the wave height. This can be easily proofed based on the three points below:

1) From Eq. (A.2.I), it readily follows that:

$$ln\left(\frac{z_{2\%}}{H_{m0,TOE}}\right) = 0.57 - 0.23 \bullet ln\left(H_{m0,TOE}\right) \quad \text{(A.2.V)}$$

2) as already shown in Fig. 14 (panel a), there is a significant relationship between $T_{m-10,\ TOE}$ and $H_{m0,TOE}$; considering the entire van Gent's dataset, and neglecting the effect of the beach slope (Hofland et al., 2017), the following equation can be established:

$$ln\left(H_{m0,TOE}\right) = -1.55 - 0.91 \bullet ln\left(T_{m-10,TOE}\right) \quad \text{(A.2.VI)}$$

which is shown in panel a of Figure A.2.2.

3) by eliminating the wave height from the two formulae above, we come to:

$$ln\left(\frac{z_{2\%}}{H_{m0,TOE}}\right) = 0.93 + 0.21 \bullet ln\left(T_{m-10,TOE}\right) \quad \text{(A.2.VII)}$$

which represents a "spurious relationship" between $\frac{z_{2\%}}{H_{m0,TOE}}$ and $T_{\text{m-10,TOE}}$. Indeed, it does not express an actual (physical) link between the variables but a statistical artifact generated (artificially) by the correlation between $H_{\text{m0,TOE}}$ and $T_{\text{m-10,TOE}}$.

The equation (A.2.VII) is shown in panel b of Figure A.2.2, where it reasonably fits the data despite some nonlinearity due to the simplifications adopted in the analysis.

Because of the strong influence of the wave height on wave runup, the spurious model results in an R^2 statistics relatively high (0.48), much higher than the actual "period variable" $T_{\text{p,off}}$, which appears as a weaker predictor ($R^2 = 0.25$, panel c).

Finally, it is essential to note that $\frac{z_{2\%}}{H_{m0,TOE}}$ is almost uncorrelated with T_{01} in panel d.

This result is nothing but the effect of the saturation of the PSD's first-order moment shown in Fig. 11c; as discussed in the paper, this saturation weakens the relationship between T_{01} and $H_{\text{m0,TOE}}$ (Fig. 14, panel b) and prevents the spurious correlation structure. In other words, since there is no relationship between T_{01} and $H_{\text{m0,TOE}}$, there will be no correlation between T_{01} and $\frac{z_{2\%}}{H_{m0,TOE}}$.

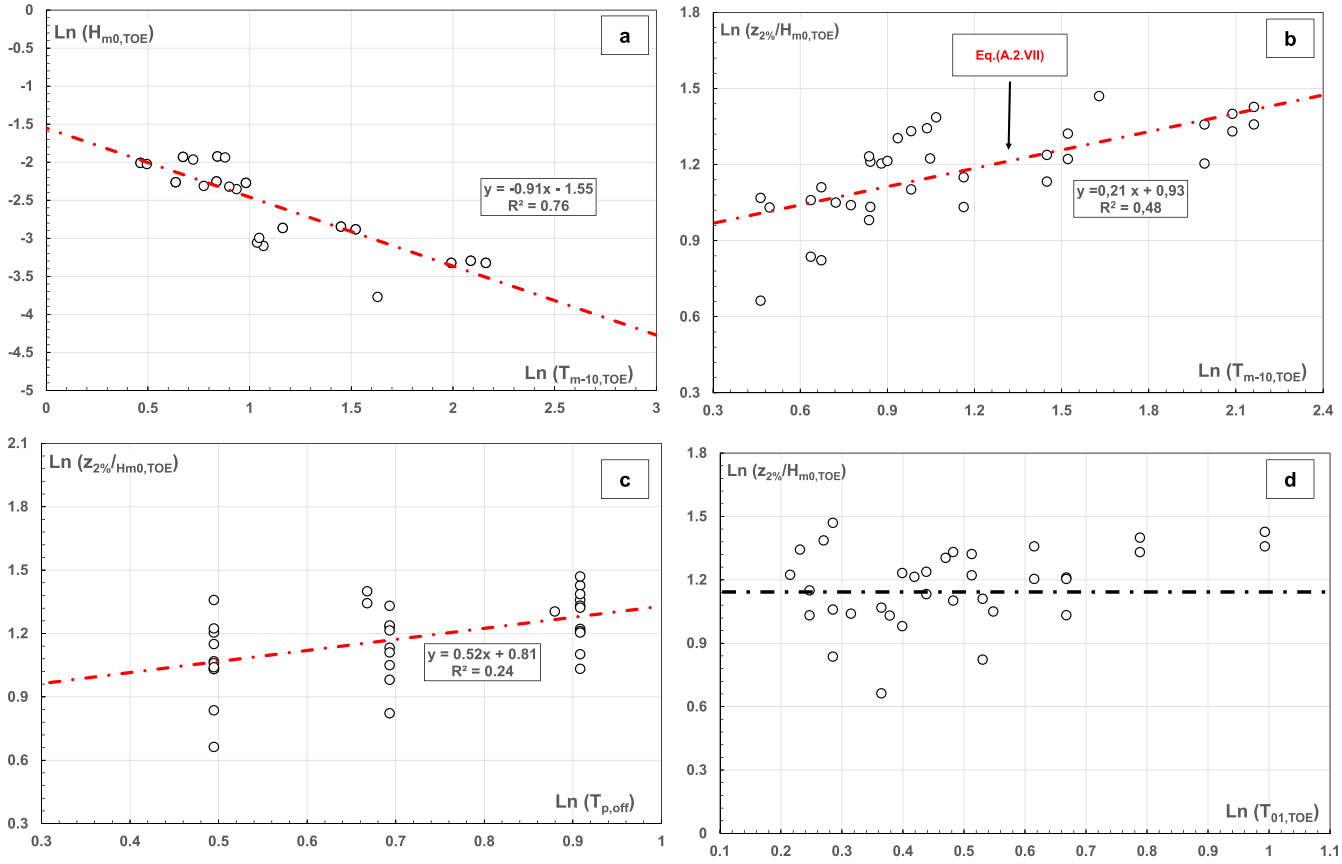

Figure A.2.2. Spurious correlation effects in the analysis of van Gent's runup data.

References

Abolfathi, S., Shudi, D., Borzooei, S., Yeganeh-Bakhtiari, A., Pearson, J., 2018. Application of smoothed particle hydrodynamics in evaluating the performance of coastal retrofit structures. Coas. Eng. Proc. 1 (36), 109. https://doi.org/10.9753/icce.v36.papers.109.

Aggarwal, A., Chella, M.A., Bihs, H., Myrhaug, D., 2020. Properties of breaking irregular waves over slopes. Ocean Eng. 216, 108098 https://doi.org/10.1016/j.oceaneng.2020.108098.

Akbari, H., 2017. Simulation of wave overtopping using an improved SPH method. Coast. Eng. 126, 51–68. https://doi.org/10.1016/j.coastaleng.2017.04.010.

Akbari, H., Pooyarad, A., 2020. Wave force on protected submarine pipelines over porous and impermeable beds using SPH numerical model. Appl. Ocean Res. 98, 102118 https://doi.org/10.1016/j.apor.2020.102118.

Altomare, C., Suzuki, T., Chen, X., Verwaest, T., Kortenhaus, A., 2016. Wave overtopping of sea dikes with very shallow foreshores. Coast. Eng. 116, 236–257. https://doi.org/10.1016/j.coastaleng.2016.07.002.

Altomare, C., Gironella, X., Suzuki, T., Viccione, G., Saponieri, A., 2020. Overtopping metrics and coastal safety: a case of study from the Catalan coast. J. Mar. Sci. Eng. 8 (8), 556. https://doi.org/10.3390/jmse8080556.

Altomare, C., Gironella, X., Crespo, A.J., 2021. Simulation of random wave overtopping by a WCSPH model. Appl. Ocean Res. 116, 102888 https://doi.org/10.1016/j.apor.2021.102888.

Bahmanpouri, F., Daliri, M., Khoshkonesh, A., Namin, M.M., Buccino, M., 2021. Bed compaction effect on dam break flow over erodible bed; experimental and numerical modeling. J. Hydrol. 594, 125645 https://doi.org/10.1016/j.jhydrol.2020.125645.

Battjes, J.A., Janssen, J.P.F.M., 1978. Energy loss and set-up due to breaking of random waves. Coast. Eng. 1978, 569–587.

Besley, P., 1999. Overtopping of seawalls—design and assessment manual. In: R&D Technical Report W 178. Environment Agency, UK.

Boers, M., 1996. Simulation of a Surf Zone with a Barred Beach; Part 1: Wave Heights and Wave Breaking. Communication on Hydraulic and Geotechnical Engineering. Delft University of Technology, Delft, The Netherlands. Report no. 96-5.
Bradford, S.F., 2000. Numerical simulation of surf-zone dynamics. J. Waterw. Port, Coast. Ocean Eng. 126 (1), 1–13. https://doi.org/10.1061/(ASCE)0733-950X(2000)126:1(1).
Bruce, T., van der Meer, J.W., Franco, L., Pearson, J.M., 2009. Overtopping performance of different armour units for rubble mound breakwaters. Coast. Eng. 56, 166–179. https://doi.org/10.1016/j.coastaleng.2008.03.015.
Buccino, M., Del Vita, I., Calabrese, M., 2013. Predicting wave transmission past reef ball submerged breakwaters. J. Coast. Res. SI 65, 171–176. ISSN: 0749-0208.
Buccino, M., D'Anna, M., Calabrese, M., 2018. A study of wave reflection based on the maximum wave momentum flux approach. Coast. Eng. J. Taylor and Francis. https://doi.org/10.1080/05785634.2017.1418796. ISSN: 2166-4250.
Buccino, M., Daliri, M., Dentale, F., Di Leo, A., Calabrese, M., 2019a. CFD experiments on a low crested sloping top caisson breakwater. Part 1. nature of loadings and global stability. Ocean Eng. 182, 259–282. https://doi.org/10.1016/j.oceaneng.2019.04.017.
Buccino, M., Daliri, M., Dentale, F., Calabrese, M., 2019b. CFD experiments on a low crested sloping top caisson breakwater. Part 2. Analysis of plume impact. Ocean Eng. 173, 345–357. https://doi.org/10.1016/j.oceaneng.2018.12.065.
Crest Level Assessment of Coastal Structures by Full Scale Monitoring, Neural Network Prediction and Hazard Analysis on Permissible Wave Overtopping. Fifth Framework Programme of the EU, Contract n. EVK3-CT-2001-00058..
den Bieman, van Gent, van den Boogaard, 2021. Wave overtopping predictions using an advanced machine learning technique. Coast. Eng. 166, 103830. https://doi.org/10.1016/j.coastaleng.2020.103830.
Dong, S., Abolfathi, S., Salauddin, M., Pearson, J., 2020. Spatial distribution of wave-by-wave overtopping at vertical seawalls. Coas. Eng. Proc. 17 (36v) https://doi.org/10.9753/icce.v36v.structures.17 structures.
Dong, S., Abolfathi, S., Salauddin, M., Pearson, J.M., 2021a. Spatial distribution of wave-by-wave overtopping behind vertical seawall with recurve retrofitting. Ocean Eng. 238, 109674 https://doi.org/10.1016/j.oceaneng.2021.109674.
Dong, S., Salauddin, M., Abolfathi, S., Pearson, J., 2021b. Wave impact loads on vertical seawalls: effects of the geometrical properties of recurve retrofitting. Water 13 (20), 2849. https://doi.org/10.3390/w13202849.
Draper, N.R., Smith, N., 1998. Applied Regression Analysis 1–716. https://doi.org/10.1002/9781118625590. http://onlinelibrary.wiley.com/book/10.1002/9781118625590. ISBN: 978-111862559-0; 978-111862568-2.
EurOtop, 2018. Manual on wave overtopping of sea defences and related structures. In: Van der Meer, J.W., Allsop, N.W.H., Bruce, T., De Rouck, J., Kortenhaus, A., Pullen, T., Schüttrumpf (Eds.), An Overtopping Manual Largely Based on European Research, but for Worldwide Application.
Flow Science, Inc, 2009. In: Santa Fe, N.M. (Ed.), FLOW-3D User's Manual, HYDRO edition. Flow Science, Inc.
Formentin, S., Palma, G., Zanuttigh, B., 2021. Integrated assessment of the hydraulic and structural performance of crown walls on top of smooth berms. Coast. Eng. 168, 103951 https://doi.org/10.1016/j.coastaleng.2021.103951.
Franco, C., Franco, L., 1999. Overtopping formulas for caisson breakwaters with nonbreaking 3D waves. J. Waterw. Port, Coast. Ocean Eng. 125 (2), 98–108. https://doi.org/10.1061/(ASCE)0733-950X(1999)125:2(98.
Franco, L., De Gerloni, M., Van der Meer, J.W., 1994. Wave overtopping on vertical and composite breakwaters. Coast. Eng. 1030–1045. https://doi.org/10.1061/9780784400890.076.
Goda, Y., 1975. Irregular wave deformation in the surf zone. Coast. Eng. Jpn. 18 (1), 13–26. https://doi.org/10.1080/05785634.1975.11924196.
Goda, Y., 2000. Random seas and design of maritime structures. In: Vol. 15 of Advanced Series on Ocean Engineering, second ed. World Scientific, Singapore.
Goda, Y., 2009. Derivation of unified wave overtopping formulas for seawalls with smooth, impermeable surfaces based on selected CLASH datasets. Coast. Eng. 56 (4), 385–399. https://doi.org/10.1016/j.coastaleng.2008.09.007.
Goda, Y., Kishara, Y., Kamiyama, Y., 1975. Laboratory Investigation on the Overtopping Rate of Seawalls by Irregular Waves. Report of the Port and Harbour Research Institute.
Habib, M.A., O'Sullivan, J.J., Abolfathi, S., Salauddin, M., 2023. Enhanced wave overtopping simulation at vertical breakwaters using machine learning algorithms. PLoS One 18 (8), e0289318. https://doi.org/10.1371/journal.pone.0289318.
Hansen, W., 1956. Theorie zur Errechnung des Wasserstandes und der Strömingen in Randmeeren nebst Anwendungen. Tellus 8, 289–300.
Hedges, T.S., Reis, M.T., 1998. Random wave overtopping of simple seawalls: a new regression model. Proc. Inst. Civil Eng. Water Marit. Energy 130 (1), 1–10. https://doi.org/10.1680/iwtme.1998.30223.
Henderson, S.M., Bowen, A.J., 2002. Observations of surf beat forcing and dissipation. J. Geophys. Res. 107 https://doi.org/10.1029/2000JC000498, 14-1-14-10.
Hirt, C.W., Nichols, B.D., 1981. Volume of fluid (VOF) method for the dynamics of free boundaries. J. Comput. Phys. 39 (1), 201–225. https://doi.org/10.1016/0021-9991(81)90145-5.
Hofland, B., Chen, X., Altomare, C., Oosterlo, P., 2017. Prediction formula for the spectral wave period Tm-1, 0 on mildly sloping shallow foreshores. Coast. Eng. 123, 21–28. https://doi.org/10.1016/j.coastaleng.2017.02.005.
Kamphuis, J.W., 1991. Incipient wave breaking. Coast. Eng. 15 (3), 185–203. https://doi.org/10.1016/0378-3839(91)90002-X.
Kamphuis, J.W., 1996. Experiments on design wave height in shallow water. Proc. Int. Conf. Coast. Eng. 1, 221–232.
Koosheh, A., Etemad-Shahidi, A., Cartwright, N., Tomlinson, R., Van Gent, M.R., 2021. Individual wave overtopping at coastal structures: a critical review and the existing challenges. Appl. Ocean Res. 106, 102476 https://doi.org/10.1016/j.apor.2020.102476.
Larsen, B.E., Fuhrman, D.R., 2018. On the over-production of turbulence beneath surface waves in Reynolds-averaged Navier–Stokes models. J. Fluid Mech. 853, 419–460. https://doi.org/10.1017/jfm.2018.577.
Lashley, C.H., Zanuttigh, B., Bricker, J.D., Van der Meer, J., Altomare, C., Suzuki, T., Roeber, V., Oosterlo, P., 2020. Benchmarking of numerical models for wave overtopping at dikes with shallow mildly sloping foreshores: accuracy versus speed. Environ. Model. Software 130, 104740. https://doi.org/10.1016/j.envsoft.2020.104740.
Lashley, C.H., van der Meer, J.W., Bricker, J.D., Altomare, Suzuki, Hirayama, K., 2021. Formulating wave overtopping at vertical and sloping structures with shallow foreshores using deep-water wave characteristics. J. Waterw. Port, Coast. Ocean Eng. 147 (6) https://doi.org/10.1061/(ASCE)WW.1943-5460.0000675.
Lashley, C.H., Brown, J.M., Yelland, M.J., Van der Meer, J.W., Pullen, T., 2023. Comparison of deep-water-parameter-based wave overtopping with wirewall field measurements and social media reports at Crosby (UK). Coast. Eng. 179, 104241 https://doi.org/10.1016/j.coastaleng.2022.104241.
Le Mehaute, B., 1962. On non-saturated breakers and the wave run-up. Coas. Eng. Proc. (8) 6-6.
Li, Y., Larsen, B.E., Fuhrman, D.R., 2022. Reynolds stress turbulence modelling of surf zone breaking waves. J. Fluid Mech. 937, A7. https://doi.org/10.1017/jfm.2022.92.
Lin, P., Liu, P.L.F., 1999. Internal wave-maker for Navier-Stokes equations models. J. Waterw. Port, Coast. Ocean Eng. 125 (4), 207–215. https://doi.org/10.1061/(ASCE)0733-950X(1999)125:4(207).
Lopez, L.F.C., Salerno, D., Dentale, F., Capobianco, A., Buccino, M., 2015. Experimental campaign on the overtopping of the seawall Malecòn Tradicional. In: The Twenty-Fifth International Ocean and Polar Engineering Conference. OnePetro.
Lopez, L.F.C., Salerno, D., Dentale, F., Capobianco, A., Buccino, M., 2016. Wave overtopping at Malecòn tradicional, la Habana, Cuba. Coas. Eng. Proc. 35, 24-24.
Mares-Nasarre, P., Argente, G., Gómez-Martín, M.E., Medina, J.R., 2019. Overtopping layer thickness and overtopping flow velocity on mound breakwaters. Coast. Eng. 154, 103561 https://doi.org/10.1016/j.coastaleng.2019.103561.
Mares-Nasarre, P., Molines, J., Gomez-Martin, M.E., Medina, J.R., 2020. Individual wave overtopping volumes on mound breakwaters in breaking wave conditions and gentle sea bottoms. Coast. Eng. 159, 103703 https://doi.org/10.1016/j.coastaleng.2020.103703.
Mase, H., Tamada, T., Yasuda, T., Hedges, T.S., Reis, M.T., 2013. Wave runup and overtopping at seawalls built on land and in very shallow water. J. Waterw. Port, Coast. Ocean Eng. 139 (5), 346–357. https://doi.org/10.1061/(ASCE)WW.1943-5460.0000199.
Nørgaard, J.Q.H., Andersen, T.L., Burcharth, H.F., Steendam, G.J., 2013. Analysis of overtopping flow on sea dikes in oblique and short-crested waves. Coast. Eng. 76, 43–54. https://doi.org/10.1016/j.coastaleng.2013.01.012.
Nørgaard, J.Q.H., Andersen, T.L., Burcharth, H.F., 2014. Distribution of individual wave overtopping volumes in shallow water wave conditions. Coast. Eng. 83, 15–23. https://doi.org/10.1016/j.coastaleng.2013.09.003.
Owen, M.W., 1980. Design of Seawalls Allowing for Wave Overtopping. Hydraulics Research, Wallingford. Report No. EX 924, UK.
O'Sullivan, J., Salauddin, M., Abolfathi, S., Pearson, J., 2020. Effectiveness of eco-retrofits in reducing wave overtopping on seawalls. Coas. Eng. Proc. (36v), 13. https://doi.org/10.9753/icce.v36v.structures.13 structures.
Pearson, J., Bruce, T., Allsop, W., Kortenhaus, A., Van der Meer, J.W., 2004. Effectiveness of recurve walls in reducing wave overtopping on seawalls and breakwaters. Coast. Eng. 4, 4404–4416. https://doi.org/10.1142/9789812701916_0355.
Reniers, Ad, Zijlema, M., 2022. SWAN SurfBeat-1D. Coast. Eng. 172, 104068 https://doi.org/10.1016/j.coastaleng.2021.104068.
Salauddin, M., O'Sullivan, J., Abolfathi, S., Dong, S., Pearson, J.M., 2020. Distribution of individual wave overtopping volumes on a sloping structure with a permeable foreshore. Coas. Eng. Proc. (36v).
Salauddin, M., O'Sullivan, J.J., Abolfathi, S., Zeng, P., Dong, S., Pearson, J.M., 2022. New insights in the probability distributions of wave-by-wave overtopping volumes at vertical breakwaters. Sci. Rep. 12, 16228 https://doi.org/10.1038/s41598-022-20464-5.
Sandoval, C., Bruce, T., 2017. Wave overtopping hazard to pedestrians: video evidence from real accidents. In: Coasts, Marine Structures and Breakwaters 2017. ICE Publishing, pp. 501–512. https://doi.org/10.1680/cmsb.63174.0501.
Sasani Babak, A., Akbari, H., 2019. Numerical study of wave run-up and overtopping considering bed roughness using SPH-GPU. Coast Eng. J. 61 (4), 502–519. https://doi.org/10.1080/21664250.2019.1647961.
Saville, T., 1955. Laboratory Data on Wave Run-Up and Overtopping on Shore Structures (No. 64). US Beach Erosion Board.
Schäffer, H., 1993. Infragravity waves induced by short-wave groups. J. Fluid Mech. 247, 551–588. https://doi.org/10.1017/S0022112093000564.
Schäffer, H.A., Jakobsen, K., 2003. Non-linear wave generation and active absorption in wave flumes. In: Long Waves Symposium. Thessaloniki, Greece.
Schäffer, H.A., Svendsen, I.A., 1988. Surf beat generation on a mild slope beach. Malaga, Spain, 1988. In: Proc. 21st Intl Conf. Coastal Engng, vol. 2. ASCE, New York, pp. 1058–1072, 1989.
Schüttrumpf, H., Van Gent, M.R., 2003. Wave overtopping at seadikes. Coast. Struct. 2003, 431–443.
Smit, P., Zijlema, M., Stelling, G., 2013. Depth-induced wave breaking in a non-hydrostatic, near-shore wave model. Coast. Eng. 76, 1–16. https://doi.org/10.1016/j.coastaleng.2013.01.008.

Suzuki, 2014. Introduction to SWASH model: theory and hands-on session. Slide available at: https://ephyslab.uvigo.es/old-site/files/7814/0379/2227/TomohiroSuzuki.pdf.

Suzuki, T., Verwaest, T., Hassan, W., Veale, W., Reyns, J., Trouw, K., Troch, P., Zijlema, M., 2011. The applicability of SWASH model for wave transformation and wave overtopping: a case study for the Flemish coast. In: Proc. 5th Int. Conf. Advanced Computational Methods Engineering. Liège, Belgium, 14-17 November.

Suzuki, T., Altomare, C., Verwaest, T., Trouw, K., Zijlema, M., 2014. Two-dimensional wave overtopping calculation over a dike in shallow foreshore by SWASH. In: ICCE 2014: Proceedings of 34th International Conference on Coastal Engineering. Coastal Engineering Research Council, Seoul, Korea, 15-20.

Suzuki, T., Altomare, C., Veale, W., Verwaest, T., Trouw, K., Troch, P., Zijlema, M., 2017. Efficient and robust wave overtopping estimation for impermeable coastal structures in shallow foreshores using SWASH. Coast. Eng. 122, 108–123. https://doi.org/10.1016/j.coastaleng.2017.01.009.

Symonds, G., Huntley, D.A., Bowen, A.J., 1982. Two-dimensional surf beat: long wave generation by a time-varying breakpoint. J. Geophys. Res. Oceans 87 (C1), 492–498. https://doi.org/10.1029/JC087iC01p00492.

Tayfun, M.A., Lo, J.M., 1989. Envelope, phase, and narrow-band models of sea waves. J. Waterw. Port, Coast. Ocean Eng. 115, 5. https://doi.org/10.1061/(ASCE)0733-950X(1989)115:5(594).

Toro, E.F., 2001. Shock-capturing Methods for Free-Surface Shallow Flows. Wiley-Blackwell.

Torres-Freyermuth, A., Lara, J.L., Losada, I.J., 2010. Numerical modelling of short-and long-wave transformation on a barred beach. Coast. Eng. 57 (3), 317–330. https://doi.org/10.1016/j.coastaleng.2009.10.013.

Torres-Freyermuth, A., Losada, I.J., Lara, J.L., 2007. Modeling of surf zone processes on a natural beach using Reynolds-Averaged Navier-Stokes equations. J. Geophys. Res.: Oceans 112 (C9).

Tucker, M.J., 1950. Surf beats: sea waves of 1 to 5 min. period. Proc. Roy. Soc. Lond. A 202, 565–573. Google Scholar.

Van der Meer, 1995. Conceptual design of rubble mound breakwaters. Adv. In Coast. Ocean Eng. 1, 221–315. https://doi.org/10.1142/9789812797582_0005.

Van der Meer, J.W., Janssen, J.P., 1994. Wave run-up and wave overtopping at dikes and revetments. Delft Hydraulics, p. 22. Delft.

Van der Meer, J., Steendam, G.J., Bruce, T., Breteler, M.K., 2022. Admissible post-wave overtopping flow for persons on a horizontal surface. J. Coast. Hydraul. Struct. 2, 15. https://doi.org/10.48438/jchs.2022.0015.

Van Doorslaer, K., De Rouck, J., Audenaert, S., Duquet, V., 2015. Crest modifications to reduce wave overtopping of non-breaking waves over a smooth dike slope. Coast. Eng. 101, 69–88. https://doi.org/10.1016/j.coastaleng.2015.02.004.

Van Gent, M.R., 1999. Wave Run-Up and Wave Overtopping for Double Peaked Wave Energy Spectra, p. H3351.

Van Gent, M.R.A., van den Boogaard, H.F.P., Pozueta, B., Medina, J.R., 2007. Neural network modelling of wave overtopping at coastal structures. Coast. Eng. 54, 586–593. https://doi.org/10.1016/j.coastaleng.2006.12.001.

Victor, L., Van der Meer, J.W., Troch, P., 2012. Probability distribution of individual wave overtopping volumes for smooth impermeable steep slopes with low crest freeboards. Coast. Eng. 64, 87–101. https://doi.org/10.1016/j.coastaleng.2012.01.003.

Walkden, M.J., Wood, D.J., Bruce, T., Peregrine, D.H., 2001. Impulsive seaward loads induced by wave overtopping on caisson breakwaters. Coast. Eng. 42 (3), 257–276. https://doi.org/10.1016/S0378-3839(00)00063-6.

Wallingford, H.R., 2005. Dynamic wave absorption system. Report available at: https://www.hrwallingford.com/sites/default/files/2020-06/eq-011_multielement_wavemaker-r6.pdf.

Wei, G. (Ed.), 2015. Flow Science Report 07-15: the Sponge Layer Method in FLOW-3D. Flow Science, Inc.

Yakhot, V., Smith, L.M., 1992. The renormalization group, the ε-expansion and derivation of turbulence models. J. Sci. Comput. 7, 35.

Zanuttigh, B., Formentin, S., Van der Meer, J.W., 2016. Prediction of extreme and tolerable wave overtopping discharges through an advanced neural network. Ocean Eng. 127, 722. https://doi.org/10.1016/j.oceaneng.2016.09.032.

Zelt, J.A., Skjelbreia, J.E., 1992. Estimating incident and reflected wave fields using an arbitrary number of wave gauges. Coast. Eng. 777–789. https://doi.org/10.1061/9780872629332.058.

Zijlema, M., Stelling, G.S., 2005. Further experiences with computing non-hydrostatic free-surface flows involving water waves. Int. J. Numer. Meth. Fluids 48, 169–197. https://doi.org/10.1002/fld.821.

Zijlema, M., Stelling, G.S., 2008. Efficient computation of surf zone waves using the nonlinear shallow water equations with non-hydrostatic pressure. Coast. Eng. 55, 780–790. https://doi.org/10.1016/j.coastaleng.2008.02.020.

Zijlema, M., Stelling, G., Smit, P., 2011. SWASH: an operational public domain code for simulating wave fields and rapidly varied flows in coastal waters. Coast. Eng. 58 (10), 992–1012. https://doi.org/10.1016/j.coastaleng.2011.05.015.